Global Journal of Science Frontier Research: F
Mathematics and Decision Sciences
Volume 16 Issue 3 Version 1.0 Year 2016
Type : Double Blind Peer Reviewed International Research Journal
Publisher: Global Journals Inc. (USA)
Online ISSN: 2249-4626 & Print ISSN: 0975-5896

Effects of Nonisothermality and Wind-Shears on the Propagation of Gravity Waves (II): Ray-Tracing Images

By J. Z. G. Ma
California Institute of Integral Studies, United States

Abstract- We investigate the effects of the wind shears and nonisothermality on the ray propagation of acoustic-gravity waves in a nonhydrostatic atmosphere by generalizing *Marks & Eckermann's* WKB ray-tracing formalism (1995: J. Atmo. Sci., 52, 11, 1959-1984; cited as ME95). Five atmospheric conditions are considered, starting from the simplest isothermal and shearfree case. In every step case a set of ray equations is derived to numerically code into a global ray-tracing model and calculate the profiles of ray paths in space and time, wavelengths and intrinsic wave periods along the rays, meanfield temperature or horizontal zonal/meridional wind speeds, as well as their gradients, and the WKB criterion parameter, δ. Results include, but not limited to, the following: (1) Rays in shear-free and isothermal atmosphere follow straight lines in space; both forward and backward-mapping rays are superimposed upon each other; wavelengths ($\lambda_{x,y,z}$), as well as the intrinsic wave period (τ), keep constant versus altitude. (2) If Hines' locally isothermal condition is applied, i.e., including the effect of temperature variations in altitude, ray traces become non-straight; however, their projections in the horizontal plane keep straight; the forward and backward ray traces are no longer overlain; and, $\lambda_{x,y,z}$ show discernable changes but τ does not change. All the modulations happen at around 80-150 km altitudes.

GJSFR-F Classification : *MSC 2010: 76B15*

Strictly as per the compliance and regulations of :

Notes

Effects of Nonisothermality and Wind-Shears on the Propagation of Gravity Waves (II): Ray-Tracing Images

J. Z. G. Ma

Abstract- We investigate the effects of the wind shears and nonisothermality on the ray propagation of acoustic-gravity waves in a nonhydrostatic atmosphere by generalizing *Marks & Eckermann*'s WKB ray-tracing formalism (1995: J. Atmo. Sci., 52, 11, 1959-1984; cited as ME95). Five atmospheric conditions are considered, starting from the simplest isothermal and shearfree case. In every step case a set of ray equations is derived to numerically code into a global ray-tracing model and calculate the profiles of ray paths in space and time, wavelengths and intrinsic wave periods along the rays, meanfield temperature or horizontal zonal/meridional wind speeds, as well as their gradients, and the WKB criterion parameter, δ. Results include, but not limited to, the following: (1) Rays in shear-free and isothermal atmosphere follow straight lines in space; both forward and backward-mapping rays are superimposed upon each other; wavelengths ($\lambda_{x,y,z}$), as well as the intrinsic wave period (τ), keep constant versus altitude. (2) If Hines' locally isothermal condition is applied, i.e., including the effect of temperature variations in altitude, ray traces become non-straight; however, their projections in the horizontal plane keep straight; the forward and backward ray traces are no longer overlain; and, $\lambda_{x,y,z}$ show discernable changes but τ does not change. All the modulations happen at around 80-150 km altitudes. If the temperature constraint is relaxed to the nonisothermal condition by adding the effect of temperature gradients in x, y, z and t, the results do not exhibit perceptible differences. (3) If the atmosphere is only isothermal, rays are violently modulated by the zonal and meridional winds, and their shears in z, as well as gradients in x, y, t particularly during the 80-150 km altitudes where $\lambda_{x,y,z}$ and τ exhibit the most conspicuous modifications. More importantly, the forward and the backward rays never propagate along the same paths. If the isothermal condition is updated to the nonisothermal one by adding the effects of temperature gradients in x, y, z and t, modulations of the physical parameters in 0-80 km altitudes become significant. (4) While the WKB δ is below 0.4 in the Hines' model, it can be driven to close to 3 by the wind shears and nonisothermality in realistic atmosphere. In addition to the above, features of ray propagations under different initial wavelengths are also discussed.

I. Introduction

Gravity stratifies atmosphere and modifies the propagation of acoustic wave through a restoring force, namely, the buoyancy force, leading to the formation of acoustic-gravity wave, consisting of relatively higher-frequency acoustic and lower-frequency gravity branches (*Lamb* 1908; 1910). This force produces atmospheric oscillations featured by the buoyancy frequency, ω_b (isothermal condition) or ω_B (nonisothermal condition), also well-known as the Brunt-Väisälä frequency, satisfying (*Väisälä* 1925; *Brunt* 1927; *Eckart* 1960; *Hines* 1960; *Tolstoy* 1963)

$$\omega_b^2 = (\gamma - 1)\frac{g^2}{C^2}, \text{ or } \omega_B^2 = (\gamma - 1)\frac{g^2}{C^2} + \frac{g}{C^2}\frac{\mathrm{d}C^2}{\mathrm{d}z} \tag{1}$$

Author: *California Institute of Integral Studies, San Francisco, CA, USA. e-mail: zma@mymail.ciis.edu*

where γ is the adiabatic index; g is the gravitational constant; C is the speed of sound, and z is the vertical coordinate of the atmospheric frame of reference.

Acoustic-gravity waves were firstly found to be responsible for ionospheric ripples (*Hines* 1960), a traveling disturbance in space plasmas which causes the fading of radio signals (e.g., *Mimno* 1937; *Pierce & Mimno* 1940; *Munro* 1950, 1958; *Martyn* 1950; *Toman* 1955; *Heisler* 1958; *Hooke* 1968). In essence, the upward propagating waves are amplified by the exponential decrease in atmospheric density so as to trigger observable impulsive vertical undulations in Earth's atmosphere, transfer momentum and energy to plasma particles in ionosphere, and bring about detectable variations in parameters like, electron density (*Hines* 1972; *Peltier & Hines* 1976). This model was supported by a bulk of experiments (e.g., *Gershman & Grigor'ev* 1968; *Vasseur et al.* 1972; *Francis* 1974), e.g., the ionospheric observations following nuclear detonations in the atmosphere (*Hines* 1967; *Row* 1967). Tens of years of theoretical and experimental studies exposed that the possible origin of the waves also included other natural or artificial sources like, solar-wind irregularities, solar eclipses, meteors, polar and equatorial electrojets, rocket launches, thunderstorms, cold waves, tornadoes, tropical cyclones, vortexes, volcanic eruptions, tsunamis, earthquakes (e.g., *Bolt* 1964; *Harkrider* 1964; *Pierce & Coroniti* 1966; *Cole & Greifinger* 1969; *Tolstoy & Lau* 1971; *Francis* 1975; *Richmond* 1978; *Röttger*, 1981; *Huang et al.* 1985; *Fovell et al.* 1992; *Igarashi et al.* 1994; *Calais et al.* 1998; *Wan et al.* 1998; *Grigorev* 1999; *Šauli & Boška* 2001; *Fritts & Alexander* 2003, *Kanamori* 2004). Unexpectedly, space experiments confirmed that the excited waves were intrinsically linked to chemical processes in the airglow emissions in thermosphere, such as the hydroxyl (OH) nightglow fluctuations (e.g., *Krassovsky* 1972; *Peterson* 1979; *Walterscheid et al.* 1986), the 6300 Å redline (e.g., *Sobral et al.* 1978; *Hines & Tarasick* 1987; *Mendillo et al.* 1997; *Kubota et al.* 2001), and the far-ultraviolet 1356 Å emission (e.g., *Paxton et al.* 2003; *DeMajistre et al.* 2007).

The pioneer theoretical studies on acoustic-gravity waves happened during the 1950s and 1960s, when rudimentary theories and myriad effects of the waves had been investigated, as recorded by *Gossard & Munk* (1954); *Eckart* (1960); *Tolstoy* (1963); *Journal of Atmospheric and Terrestrial Physics* (1968); *Georges* (1968); *AGARD* (1972), and *Francis* (1975). Since then, particularly after the 1980s with the aid of ground-based and space-based measurements (e.g., radar, GPS), the understanding on the wave physics and its role played in the interactions between atmosphere and ionosphere have been made considerable progress (see details in, e.g., *Fritts* 1984,1989; *Hocke & Schlegel* 1996; *Fritts & Alexander* 2003; *Fritts & Lund* 2011). The advances rely dominantly on three kinds of approaches: (1) WKB (Wentzel-Kramers-Brillouin) approximation; (2) full-wave formulation; and (3) ray-tracing mapping. All of these methods intend to obtain solutions of respective set of perturbation equations originated from the same set of Navier-Stokes equations of the atmosphere under different conditions, based on the problems concerned.

Initiated by *Hines* (1960), WKB modeling draws the most attention due to its effectiveness to provide the vertical profiles of atmospheric perturbations by assuming the horizontal components of parameters, as well as the background atmosphere, change only slowly over the wave cycles of the vertical variations (*Pitteway & Hines* 1963; *Einaudi & Hines* 1970; *Hines* 1974; *Beer* 1974; *Gill* 1982; *Hickey & Cole* 1988; *Nappo* 2002; *Vadas* 2007), while the variation (k_m) of the vertical wavenumber (m) in altitude (z), $k_m = \partial(\ln m)/\partial z$,

Notes

is much smaller than m, i.e., $\delta = k_m/m \ll 1$; for large δ, this condition was assumed broken and waves were generally suggested reflected vertically (e.g., *Marks* & *Eckermann* 1995; cited as ME95 hereafter). The WKB approximation makes it valid to apply Taylor expansion to the set of Navier-Stokes equations of continuity, momentum, and energy, by assuming the solutions have the form of $\sim \exp[\pm i(kx + ly + mz - \omega t) + z/(2H)]$, where x and y are horizontal coordinates in the zonal and meridional directions, respectively, with corresponding wavenumbers k and l, H is the scale height, t is time, and ω is the ground-relative (Eulerian) wave angular frequency (e.g., *Hines* 1963; *Midgley* & *Liemohn* 1966; *Volland* 1969; *Francis* 1973; *Hickey* & *Cole* 1987; *Holton* 1992; *Fritts* & *Alexander* 2003). Neglecting ion-drag, viscosity and molecular diffusion below 200 km altitude, and using Hines' locally isothermal atmosphere which is horizontally uniform with background wind U along x and V along y, which are all shear-free in z, a classical dispersion equation can be obtained as follows (*Eckart* 1960; *Eckermann* 1997):

$$\Omega^2 \left(k_h^2 + k_z^2 - \frac{\Omega^2 - f^2}{C^2} \right) = \omega_b^2 k_h^2 + f^2 k_z^2 \tag{2}$$

where $\Omega = \omega - kU - lV$ is the intrinsic frequency, $f = 2\Omega_E \sin\phi$ is the Coriolis parameter (Ω_E is Earth's rotation rate and ϕ is latitude), $k_h^2 = k^2 + l^2$, $k_z^2 = m^2 + 1/(4H^2)$.

For the dissipative terms, *Pitteway* & *Hines* (1963) took advantage of a complex dispersion equation to confirm that they do contribute non-negligible effects at meteor heights. Besides, the shear-related Richardson number R_i was verified to provide a criterion, $R_i \sim 1/4$, which is a necessary but not sufficient condition for dynamic instability; however, this criterion might not rigorously apply to cases where the wind shear is tilted from zenith or when the molecular viscosity is important (*Hines* 1971; *Dutton* 1986; *Sonmor* & *Klaassen* 1997; *Liu* 2007). What is more, if more nonhydrodynamic terms (such as ion-drag) are included, the complexity of solving the perturbed equations made it hard to give as simple an expression of the dispersion relation as Eq.(2). Instead, *Francis* (1973); *Hickey* & *Cole* (1987) suggested a polynomial equation to demonstrate the dispersive properties of acoustic-gravity waves in the absence of wind shears, $\sum_j D_j R^j = 0$, where function R in the square of the complex vertical wave number, $\kappa = m + i/(2H)$, in which m becomes a complex; D_i is complex coefficient; and j is the number of the Navier-Stokes equations. Studies showed that the mean-field winds has a filter effect on waves (*Mayr et al.* 1984, 1990); and, waves of about 15-30 min periods and 200-400 km horizontal wavelengths are able to reach as high as 300 km altitude in the presence of dissipative terms (*Sun et al.* 2007). Note that the second point was in contrast with *Vadas* & *Fritts* (2004)'s earlier argument that the waves above ~200 km are often linked to auroral sources at high latitudes.

Unlike the WKB model, the full-wave formulation provides all the solutions of the perturbed equations, not only the WKB ones, but also those that rigorously accounts for the wave reflection. The formalism made use of the tridiagonal algorithm (*Bruce et al.* 1953; *Lindzen* & *Kuo* 1969) and assumed a single monochromatic wave of the form $f(z)e^{i(\omega t - kx - ly)}$ in an inhomogeneous atmosphere from the neutral troposphere upward to the mesosphere (50-85 km in altitude; i.e., ionospheric D region), and to a maximum altitude of 800 km in the F region, where $f(z)$ is a perturbation function as a function of z (e.g., *Yeh* & *Liu* 1974; *Lindzen* & *Tung* 1976; *Hickey et al.* 1997,2000; *Liang et*

al. 1998; *Schubert et al.* 2003). Note that there was no waveforms in z. In this case, all factors existing in realistic atmosphere can be considered, such as, height-dependent mean temperature, damping term associated with ion drag, molecular viscosity and thermal conduction, the filtering of background winds; the eddy and the molecular diffusion of heat and momentum, etc., subject to boundary conditions. The model provided the magnitude and phase of the perturbed z-dependent temperature, pressure, horizontal and vertical wind speeds (e.g., *Klostermeyer* 1972a,b,c; *Hickey et al.*, 1997, 1998, 2000, 2001; *Walterscheid* & *Hickey* 2001; *Schubert et al.* 2005). The model was not only applied to analyze Earth's acoustic waves (*Hickey et al.* 2001; *Schubert et al.* 2005; *Walterscheid* & *Hickey* 2005) and gravity waves (*Hickey et al.* 1997; *Walterscheid* & *Hickey* 2001), but also used for gravity-wave heating and cooling in Jupiters thermosphere (*Hickey et al.* 2000; *Schubert et al.* 2003).

By contrast, ray-tracing mapping is theoretically based on the WKB approximation. It comes from Fermat's principle in terms of Hamiltonian equations (*Landau* & *Lifshitz* 1959; *Whitham* 1961; *Yeh* & *Liu* 1972). In the application to acoustic-gravity waves, it formulates the spatial and temporal evolutions of a wave packet in a background wind with velocity $\mathbf{v}_0$, constrained by the WKB-approximated dispersion relation, $\omega = \omega(\mathbf{x}, \mathbf{k})$, where ω is the ground-based Eulerian or extrinsic wave frequency, $\mathbf{x}$ and $\mathbf{k}$ are the 3D position and wavenumber vectors, respectively (e.g., *Jones* 1969; *Lighthill* 1978; ME95; *Ding et al.* 2003). After *Hines* (1960) suggested that the upward propagating gravity waves can be reflected or refracted by mean-field winds, and, *Thome* (1968); *Francis* (1973) proposed that zero and higher order gravity wave modes under different isothermal conditions are able to travel horizontally as far as thousands of km, *Cowling et al.* (1971) discussed the background wind effects on the ray paths and proposed a directional filtering model. The authors argued that if gravity waves go along the winds, the intrinsic frequency is shifted downward; If the waves propagate against the winds, reflection may appear. *Yeh* & *Webb* (1972) and *Waldock* & *Jones* (1984) confirmed the filtering effect exerted by the winds on waves in a stratified atmosphere. The reflection was found to occur when wave propagate against wind; and, it is impossible for the waves to penetrate through either along or against high-speed winds. These studies were extended in a wider scope. For example, *Bertin et al.* (1975) adopted a reverse ray-tracing model to study the mechanism of wave excitation by wind perturbations in a jet stream bordering the polar front. *Waldock* & *Jones* (1984) considered the diurnal variation of the wind in the ray-tracing method. *Zhong et al.* (1995) examined the wind influence on the propagation of gravity waves in different seasons, and extended the ray-tracing simulations by including the tidal wind that has temporal and vertical variations in the study of the wave propagation through the middle atmosphere.

Particularly, ME95 set up a generalized, 3D WKB ray-tracing model to accommodate gravity waves of all frequencies in a rotating, stratified, compressible, but isothermal, nondissipative atmosphere. The nonhydrostatic model took advantage of three derived equations in dispersion, refraction, and amplitude, where excluded were wind shears, temperature gradients, and time-dependent components of the mean-field parameters. Based on Hines' locally isothermal dispersion relation, the authors exposed that the decrease in the horizontal wavenumber causes the reduction in the high-frequency cutoff; turbulent damping is more important than scale-related radiative damping; and climatological planetary waves heavily modulate ray paths of waves launched from different longitudes. After ME95's contribution, *Ding et al.* (2003) employed the same Hines' model and adopted the HWM93 wind & MSISE90 atmospheric models (*Hedin* 1991; *Hedin et al.* 1991) for

a detailed investigation on the relation between the waves and the winds. They obtained that, in response to the directions of the winds, waves are divided into three types: cut-off, reflected, and propagating; and, the ray paths of the waves can be horizontally prolonged, vertically steepened, reflected, or critically coupled. A more recent work was done by Wrasse et al. (2006) in the absence of dissipative terms. The authors followed ME95's study and derived reverse ray-tracing equations to estimate the sources of the gravity wave disturbances from wave signatures observed at 23°S (Brazil) and 7°S (Indonesia) by airglow imagers.

Notes

However, acoustic-gravity waves are so complicated in their propagation through the atmosphere that it is important to take into account convection, wind shear, dissipation, sources of transport in heat, momentum, and constituents (*Fritts & Alexaander* 2003). It is thus important to develop Hines' isothermal dispersion relation to a more general one which is able to expose the influences of factors like temperature gradient, Coriolis force, wind shear, molecular viscosity, thermal diffusivity, and ion-drag, in order to, on the one hand, understand the damping mechanism and physical effects of the waves in the coupling between atmosphere and ionosphere; on the other hand, validate and/or provide a reference to the numerical full-wave solutions. Toward this goal, an influential advance has been achieved in a series of contributions on isothermal and shear-free, but dynamically viscous and thermally diffusive atmosphere by *Vadas & Fritts* (2001, 2004, 2005, 2009). The work was recognized as the "*Vadas-Fritts* ray-tracing model" (cited as VF model hereafter), which consists of a near-field Fourier-Laplace integral representation for the around the convective source region, where rays are launched with initial conditions deduced there, and a far-field ray-tracing mapping for the propagation of the gravity waves binned in space-time grid cells, and the path of each ray is determined by its spectral amplitude and by the local density of rays within the grid cells (see details in Section 2 of *Broutman & Eckermann* 2012).

Said study improved over past efforts on WKB ray-tracing technique. Unlike using the traditional "complex-m approach" usually used in atmospheric physics by assuming a complex vertical wave number $(m_r + im_i)$ and a real wave frequency ω in, e.g., *Pitteway & Hines* (1963), the VF model adopted a "complex-ω approach" which is always employed in plasma physics by incorporating a complex wave frequency $(\omega_r + i\omega_i)$ but a real m into the dispersion relation. Otherwise, the authors claimed that the derived compressible, complex, dispersion equation, equipped with terms of molecular viscosity (ν) and thermal diffusivity (incorporated in the Prandtl number Pr), was unable to be solved. Though via a different approach, the model led to similar results as those obtained by *Pitteway & Hines* (1963), such as, wave damping by thermal conduction is the same order as viscous damping; amplitude of perturbations in an inviscid atmosphere always keeps constant, in addition to the factor of $1/(2H)$, regardless of any positions in space; in a viscid atmosphere, the wave growth depends entirely on ν. More significantly, the authors found that waves in high frequencies and large vertical wavelengths will propagate to high altitudes, and it is the integrated viscosity effect, rather than the local value of viscosity, that determines wave dissipation; molecular viscosity and thermal diffusivity act as filters on the wave spectrum, allowing only those high-frequency, large vertical wavelength waves to propagate up to high altitudes. The model was assumed not only to interpret measurements such as the airglow data near 85 km altitude (*Vadas et al.* 2009), but also to explain the ionospheric soundings near 250 km altitude (*Vadas & Crowley* 2010).

The achievements introduced above under isothermal and shear-free conditions are of great importance for us to gain fundamental understandings on the physics of generalized

acoustic-gravity waves, and then, based on this knowledge, to take incremental steps for suitable solutions of more realistic problems. Such a problem has arisen in last 15 years since lidar facilitates recorded both large wind shears (e.g., 100 m/s per km) and large temperature gradient (up to 100 °K per km) between ∼85 and 95 km altitudes (*Liu et al.* 2002; *Fritts et al.* 2004; *Franke et al.* 2005; *She et al.* 2006, 2009). Spaceborne data also confirmed that the criterion of wind-shear related Richardson number, $R_i \leq 1/4$, appeared to reach 1 at 90 km altitude over Svalbard (78°N, 16°E; *Hall et al.* 2007); and, measurements of airglow layer perturbations in O(^{1}S) (peak emission altitude ∼97 km) and OH (peak emission altitude ∼87 km) driven by propagating acoustic-gravity waves suggested that the factor of $1/(2H)$ should be modified by $(1-\beta)/(2H)$, where β is the so-called "damping factor" (*Liu & Swenson* 2003; *Vargas et al.* 2007). This parameter is positive, varying between 0.2 and 1.69 with a stronger positive correlation with the meridional wind shear than the zonal one, and a positive correlation for waves of shorter than 40 km vertical wavelengths, while a negative correlation for longer ones (*Ghodpage et al.* 2014). Considering the fact that both the ion drag and Coriolis force can be neglected below 600 km (*Volland* 1969), and viscosity can also be omitted as compared with heat conductivity within the same heights, while below about 200 km the later itself turns out to be evanescent (*Harris & Priester* 1962; *Pitteway & Hines* 1963; *Volland* 1969), influences by both wind shears and nonisothermality were consequently regarded as the candidates to exert impacts on the propagation of gravity waves through realistic mesosphere and lower thermosphere. The most recent study by *Ma et al.* (2014) exposed that (1) Wind shears and nonisothermality modulate Hines' model in both real and imaginary vertical wavenumbers. While negligible below 80 km altitude, the modulation is appreciable above 80 km altitude. It drives the atmosphere into a "sandwich" structure with three layers: 80-115 km, 115-150 km, and 150-200 km. (2) "Damping factor", β, keeps positive in the top and bottom layers where wave attenuations (damping effect) appear, while it is negative in the middle layer where wave intensification (amplifying effect) occurs. The sign of β is determined by $\cos\theta$, where θ is the angle between the mean-field wind velocity and horizontal wave vector. (3) The strongest intensification happens at 125 km altitude at which the imaginary vertical wave-number, m_i, is - 0.25 km^{-1}; the three strongest attenuations happen at 90, 100, 180 km altitudes with m_i =+0.01, +0.03, +0.05 km^{-1}, respectively. (4) Within the acoustic and gravity wave-periods, usually no more than tens of minutes, the Coriolis effect plays an unrecognized role, whileas it affects the inertial waves, the waveperiod of which is in the order of hours.

Therefore, the isothermal and shear-free assumptions may be inadequate to be applied for a quantitative explanation of the observations in much more complicated situations in atmosphere, especially in the modeling and analyses of spaceborne data from, e.g., RADAR, GPS. Nevertheless, we argue that the formalism under previous assumptions is help ful, at least qualitatively speaking, as a good reference for us to treat realistic atmospheric situations (e.g., *Wrassea et al.* 2006) where both the temperature and wind gradients in the vertical direction are unable to be neglected, as demonstrated by the airglow measurements below 200 km altitude. It is thus necessary to take into account these important factors in ray-tracing imaging so as to have a better understanding on the propagation of acoustic-gravity waves in the presence of nonisothermality and wind shears. This paper will extend the VF model by incorporating the vertical temperature inhomogeneity and wind shear into a perturbed set of mass, momentum, and energy equations, but adopting ME95's simplification of ignoring the dissipation terms (i.e., molecular viscosity, heat source, ion drag). The negligence of these terms had already been validated by classical work of, e.g., *Harris & Priester* (1962); *Pitteway & Hines* (1963); *Volland* (1969). We follow ME95's algebra and nomenclature by taking the traditional complex-k_z approach

to manipulate dispersion equation for ray-tracing equations, rather than the complex-ω algebra used in the VF model. In order to clearly illustrate the propagating paths of 3D rays driven by diverse, localized, and intermittent sources (such as, tsunami, volcano) in realistic atmosphere, we intentionally expand the inviscid heights from 0∼200 km to 0∼300 km in ray-tracing simulations.

The structure of the paper is as follows. Section 2 develops ME95's locally isothermal ray-tracing model to a generalized set of ray-tracing equations of acoustic-gravity waves under wind-shearing and nonisothermal conditions. Section 3 presents numerical results of ray-tracing images in five different atmospheric situations, starting from the simplest isothermal and shear-free model to the most complicated nonisothermal and wind-shearing model, to expose the effects of the nonisothermality and wind shears. The vertical profile of the WKB δ parameter is also exhibited under some typical situations. Section 4 offers a quick summary and discussion. SI units are used throughout the paper, with exceptions noted wherever necessary.

Notes

II. Ray-Tracing Equations

a) Formulation

The classical formulation of ray-tracing theory is briefly described as follows. Let ω be the ground-based (Eulerian, or, extrinsic) wave frequency, $\mathbf{r} = \{x, y, z\}$ and $\mathbf{k} = \{k, l, m_r\}$ are the position vector, and wavenumber vector, respectively, where subscript "$_r$" attached to m denotes the "real" part of the vertical wavenumber m. It will be omitted for simplification throughout the rest of the text. Based on Fermat's principle in terms of Hamiltonian equations (e.g., *Landau* & *Lifshitz* 1959; *Whitham* 1961; *Yeh* & *Liu* 1972), the ray-path, Γ, of internal gravity waves are determined both spatially and temporally by the dispersion relationship, $\omega = \omega(\mathbf{r}, \mathbf{k})$ (e.g., *Jones* 1969; *Lighthill* 1978):

$$\Gamma = \Gamma(\mathbf{r}, t; \mathbf{k}, \omega) \tag{3}$$

and m is constrained by the WKB dispersion equation along the rays:

$$m = m(\mathbf{r}, t; k_h, \omega) \tag{4}$$

For any rays with a generalized phase Φ,

$$\Phi = \int_{\Gamma(t)} (\omega \mathrm{d}t - \mathbf{k} \cdot \mathrm{d}\mathbf{r}) \tag{5}$$

only those with steady phase values are able to be observed and measured. Mathematically, this requires that the variation of Φ is zero, namely,

$$\delta\Phi = \delta \int_{\Gamma(t)} G \mathrm{d}t = \delta \int_{\Gamma(t)} \left(\omega - \mathbf{k} \cdot \frac{\mathrm{d}\mathbf{r}}{\mathrm{d}t} \right) \mathrm{d}t = 0 \tag{6}$$

in which

$$G = \omega - \mathbf{k} \cdot \frac{\mathrm{d}\mathbf{r}}{\mathrm{d}t} \tag{7}$$

is a functional to be integrated. The calculus of variations provides the following set of differential equations:

$$\frac{\partial G}{\partial \omega}=0\ ,\ \frac{\partial G}{\partial \mathbf{k}}=0\ ,\ \frac{\partial G}{\partial \mathbf{r}}-\frac{\mathrm{d}}{\mathrm{d}t}\frac{\partial G}{\partial \dot{r}_t}=0 \tag{8}$$

where $\dot{r}_t=\mathrm{d}\mathbf{r}/\mathrm{d}t$. Specifically, the set of vector equations is as follows:

$$\frac{\mathrm{d}\mathbf{x}}{\mathrm{d}t}=\frac{\partial \omega}{\partial \mathbf{k}}=\frac{\partial(\Omega+\mathbf{k}\cdot\mathbf{v}_0)}{\partial \mathbf{k}},\ \text{or},\ \mathbf{c}_g=\mathbf{v}_0+\mathbf{c}_{g*} \tag{9}$$

and

$$\frac{\mathrm{d}\mathbf{k}}{\mathrm{d}t}=-\frac{\partial \omega}{\partial \mathbf{x}}=-\frac{\partial(\Omega+\mathbf{k}\cdot\mathbf{v}_0)}{\partial \mathbf{x}}=-\frac{\partial(\mathbf{k}\cdot\mathbf{v}_0)}{\partial \mathbf{x}}-\frac{\partial \Omega}{\partial \mathbf{x}} \tag{10}$$

where

$$\Omega=\omega-\mathbf{k}\cdot\mathbf{v}_0=\omega-\mathbf{k}_h\cdot\mathbf{v}_0,\quad \mathbf{c}_g=\frac{\partial \omega}{\partial \mathbf{k}},\quad \mathbf{c}_{g*}=\frac{\partial \Omega}{\partial \mathbf{k}} \tag{11}$$

are the Doppler-shifted (Lagrangian, or, intrinsic) wave frequency, the extrinsic and intrinsic group velocities, respectively, in which $\mathbf{k}_h=\{k,l\}$ and $\mathbf{v}_0=\{U,V,0\}$.

b) ME95's model and its generalization

Based on Hines (1960)'s locally isothermal and shear-free dispersion relation, ME95 developed a global WKB ray-tracing model of a set of six equations to accommodate gravity waves of all frequencies in a nonhydrostatic, rotating, stratified, and compressible atmosphere characterized by nonuniformities which are supposed to change slowly in real space (x,y,z), but keep constant in time (t), that is, wave period ($2\pi/\omega$; tens of minutes) $\ll$ Earth's daily rotation period ($1/f$ ~12 hours). As a result, the mean-field horizontal wind of velocity $\mathbf{v}_0=\{U(x,y,z),V(x,y,z),0\}$ holds $\partial U/\partial t=\partial V/\partial t=0$. The model assumed that each ray starts from an initial spatial position of specific longitude, latitude, and altitude, and both k_h and ω were supposed constant in time along ray paths due to the condition of $\partial/\partial t=0$. A set of six ray equations was obtained, as given in Eq.(A3) of ME95.

We extend ME95's model by incorporating three additional effects: (1) nonisothermal effect, i.e., $k_T\neq 0$; and (2) wind-shear effects, i.e., $\partial U/\partial z\neq 0$ and $\partial V/\partial z\neq 0$; and, (3) time-dependent effect, i.e., $\partial/\partial t\neq 0$. Consequently, not only do additional terms appear in ME95's six equations, which are related to temperature gradient and wind shears, but also a new equation to demonstrate the temporal dependence of wave frequency Ω comes into being. The set of ray equations from Eqs.(9,10) are thus expressed as follows, which generalizes ME95's Eq.(A3):

$$\left.\begin{aligned}
&\frac{\mathrm{d}x}{\mathrm{d}t}=U+c_{g*x}=U+\frac{\partial\Omega}{\partial m}\frac{\partial m}{\partial k},\ \frac{\mathrm{d}y}{\mathrm{d}t}=V+c_{g*y}=V+\frac{\partial\Omega}{\partial m}\frac{\partial m}{\partial l},\ \frac{\mathrm{d}z}{\mathrm{d}t}=c_{g*z}=\frac{\partial\Omega}{\partial m}\\
&\frac{\mathrm{d}k}{\mathrm{d}t}=-\left(k\frac{\partial U}{\partial x}+l\frac{\partial V}{\partial x}\right)-\frac{\partial\Omega}{\partial m}\frac{\partial m}{\partial x},\ \frac{\mathrm{d}l}{\mathrm{d}t}=-\left(k\frac{\partial U}{\partial y}+l\frac{\partial V}{\partial y}\right)-\frac{\partial\Omega}{\partial m}\frac{\partial m}{\partial y},\\
&\frac{\mathrm{d}m}{\mathrm{d}t}=-\left(k\frac{\partial U}{\partial z}+l\frac{\partial V}{\partial z}\right)-\frac{\partial\Omega}{\partial m}\frac{\partial m}{\partial z},\ \frac{\mathrm{d}\Omega}{\mathrm{d}t}=\frac{\partial\Omega}{\partial m}\frac{\partial m}{\partial t}
\end{aligned}\right\} \tag{12}$$

Notes

c) Ray equations under nonisothermal and wind-sheared conditions

Instead of Eq.(1b) in ME95, which was rewritten from Eq.(2) in the Introduction of this paper, the dispersion relation used in Eq.(12) is updated to the generalized expression as given by Eq.(12) of *Ma et al.* (2014):

$$m^2 = \frac{\Omega^2 - \omega_A^2}{C^2} + k_h^2 \left[\frac{\omega_B^2 - \Omega^2}{\Omega^2} - \frac{1}{2}\frac{\omega_{\mathrm{v}}^2}{\Omega^2} \left(\frac{2-\gamma}{\gamma} \frac{\Omega^2}{k_h^2 V_p V_{ph}} + \frac{1}{2}\cos\theta \right) \cos\theta \right] \tag{13}$$

in which

$$\left.\begin{array}{l} \omega_A^2 = \omega_a^2 + g k_T,\ C^2 = \gamma \frac{k_B T_0}{M},\ \omega_{\mathrm{v}} = \sqrt{\left(\frac{\mathrm{d}U}{\mathrm{d}z}\right)^2 + \left(\frac{\mathrm{d}V}{\mathrm{d}z}\right)^2},\ \cos\theta = \frac{\mathbf{k}_h \cdot \mathbf{v}_0}{k_h \sqrt{U^2+V^2}} \\ V_p = \frac{\omega_{\mathbf{v}}}{k_p},\ V_{ph} = \frac{\Omega}{k_h};\ \text{and},\ \omega_a^2 = \frac{\gamma^2}{4(\gamma-1)}\omega_b^2,\ k_T = \frac{\mathrm{d}(\ln T_0)}{\mathrm{d}z},\ k_p = \frac{\mathrm{d}(\ln p_0)}{\mathrm{d}z} \end{array}\right\} \tag{14}$$

where ω_A and ω_a are the nonisothermal and isothermal cut-off frequencies, respectively; k_T and k_p are the scale numbers in temperature and pressure, respectively; k_B is Boltzmann's constant; T_0 is the mean-field temperature; M is the mean molecular mass of atmosphere; ω_{v} is the synthesized wind shear; θ is the angle between $\mathbf{k}_h$ and $\mathbf{v}_0$; V_p is a quasi-phase speed related to ω_{v} and k_p, and V_{ph} is the horizontal quasi-phase speed. Note that the f-terms are omitted due to their negligible roles played in the band of gravity waves. Applying Eq.(13) to Eq.(12) produces a set of generalized, nontrivial ray-tracing equations as follows, where the algebra involved is notoriously tedious but straightforward:

$$\left.\begin{array}{l} \frac{\mathrm{d}x}{\mathrm{d}t} = U - A_{11}k + A_{12}\frac{\partial U}{\partial z},\ \frac{\mathrm{d}y}{\mathrm{d}t} = V - A_{11}l + A_{12}\frac{\partial V}{\partial z},\ \frac{\mathrm{d}z}{\mathrm{d}t} = \frac{\Omega^2}{\Omega^2 - \omega_B^2}A_{11}m \\ \frac{\mathrm{d}k}{\mathrm{d}t} = -\left(k\frac{\partial U}{\partial x} + l\frac{\partial V}{\partial x}\right) - A_{22}k_c,\ \frac{\mathrm{d}l}{\mathrm{d}t} = -\left(k\frac{\partial U}{\partial y} + l\frac{\partial V}{\partial y}\right) - A_{22}l_c \\ \frac{\mathrm{d}m}{\mathrm{d}t} = -\left(k\frac{\partial U}{\partial z} + l\frac{\partial V}{\partial z}\right) - A_{22}m_c,\ \frac{\mathrm{d}\Omega}{\mathrm{d}t} = -A_{21}\left(k\frac{\partial U}{\partial t} + l\frac{\partial V}{\partial t}\right) + A_{22}c_t \end{array}\right\} \tag{15}$$

in which

$$\left.\begin{array}{l} A_{11} = \left(\Omega^2 - \omega_B^2\right)\Omega C^2/A_0,\ A_{12} = -\Omega^3 C^2/(A_0 V_*) \\ A_{21} = \left(\Omega^4 - C^2 k_h^2 \omega_B^2\right)/A_0,\ A_{22} = A_{12}V_*\left(K_*^2 - k_g^2 + \frac{\omega_{\mathrm{v}}^2}{4V_{ph}^2}\cos^2\theta\right) \\ k_c = \frac{\partial(\ln C)}{\partial x},\ l_c = \frac{\partial(\ln C)}{\partial y},\ m_c = \frac{\partial(\ln C)}{\partial z},\ c_t = \frac{\partial(\ln C)}{\partial t} \end{array}\right\} \tag{16}$$

where

$$\left.\begin{array}{l} A_0 = \Omega^4 - C^2(k_h^2\omega_B^2 + K_*^2\Omega^2),\ V_* = 4V_{ph}\frac{k_h/k_p}{\frac{2-\gamma}{\gamma} + \frac{V_p}{V_{ph}}\cos\theta} \\ K_*^2 = -\frac{1}{4}k_p\frac{\omega_{\mathrm{v}}}{V_{ph}}\left(\frac{2-\gamma}{\gamma} + \frac{V_p}{V_{ph}}\cos\theta\right)\cos\theta \end{array}\right\} \tag{17}$$

Because sound speed C is determined by temperature T, we see that the nonisothermal T-effect is converted to C-effect. Clearly, Eq.(15) demonstrates that the gradients of $\{U, V, C\}$ in the 4D spacetime (3D space + 1D time) play a leading role in the development of the ray path $\{x, y, z\}$. Note that this development is also coupled with wave vector $\{k, l, m\}$. It also deserves to stress here that the above ray equations are derived under the WKB assumption. As pointed out by *Einaudi* & *Hines* (1970); *Gossard* & *Hooke* (1975); and ME95, the validity of this condition can be exhibited by a criterion parameter, δ, expressed as (e.g., ME95)

$$\delta = \frac{1}{m}\left|\frac{\partial(\ln m)}{\partial z}\right| \tag{18}$$

Under isothermal and shear-free conditions, ME95 showed that for large δ (or, equivalently, $m \to 0$) when wave approaches a caustic, the WKB approximation breaks and ray integration terminates in simulations (see ME95 for details). The feature of this parameter will also be discussed based on our calculations.

III. Numerical Results

We expose by steps the numerical calculations of ray images about the effects of wind shears and nonisothermality on the propagation of acoustic-gravity waves, starting from the simplest case and ending at the most complicated one. We consider following five atmospheric models with six simulation steps to describe the atmosphere where ray-tracing imaging calculations are performed: (1) fully isothermal, and shear-free; (2) Hines' locally isothermal and shear-free; (3) nonisothermal and shear-free; (4) fully isothermal and wind-shearing; (5) nonisothermal and wind-shearing (generalized formulation); and, (6) nonisothermal and wind-shearing (influence of initial wavelengths). Both hydrostatic and quasi-hydrostatic cases are considered in the first two situations.

a) Fully isothermal, and shear-free atmosphere

i. *Hydrostatic*

This is the simplest case: $U = V = 0$ and T (or C) is uniform in space and constant in time. Naturally, $\nabla U = \nabla V = 0$ and $\partial U/\partial t = \partial V/\partial t = 0$. Eqs.(15-17) reduce to the following:

$$\frac{\mathrm{d}x}{\mathrm{d}t} = -A_{11}k,\ \frac{\mathrm{d}y}{\mathrm{d}t} = -A_{11}l,\ \frac{\mathrm{d}z}{\mathrm{d}t} = \frac{1}{A_0^*};\ \ \frac{\mathrm{d}k}{\mathrm{d}t} = \frac{\mathrm{d}l}{\mathrm{d}t} = \frac{\mathrm{d}m}{\mathrm{d}t} = \frac{\mathrm{d}\Omega}{\mathrm{d}t} = 0 \tag{19}$$

where

$$A_0^* = \frac{A_0}{mC^2\Omega^3},\ A_{11} = \frac{\Omega C^2}{A_0}\left(\Omega^2 - \omega_b^2\right),\ A_0 = \Omega^4 - C^2\omega_b^2 k_h^2 \tag{20}$$

Eqs.(19,20) provide following equation of 3D straight rays due to the invariant nature of all the input parameters:

$$\frac{x}{k} = \frac{y}{l} = \frac{z}{m}\left(\frac{\omega_b^2}{\Omega^2} - 1\right), \quad \text{along with } \Omega = \omega \tag{21}$$

where parameters k, l, m, ω, Ω, and ω_b are all constant in time. We arbitrarily choose horizontal wavelengths of $\lambda_x = 350$ km and $\lambda_y = 50$ km and illustrate the features of ray images in Fig.1. The top panel depicts the ray path propagating in 3D space (thick line), and its three projections (thin lines) in XY/YZ/XZ planes. The two arrows indicate both forward and backward traces, respectively, which are superimposed upon each other. The bottom four smaller panels in the figure present the propagating length and altitude of the ray versus time (upper left), the vertical profiles of sound speed C (upper right), the three wavelengths λ_x, λ_y, and λ_z (lower left), and, wave period $\tau = 2\pi/\Omega$, cut-off period $\tau_a = 2\pi/\omega_a$, and buoyancy period $\tau_b = 2\pi/\omega_b$ (lower right).

As displayed in the top panel, either the forward or the backward ray is a straight line. Relative to one end, the other end is 262.89 km away along x and 1840.2 km away along y. Clearly, $x/y = k/l$, following Eq.(21). The lapse of time that the ray travels between the two ends is given in the upper left panel of the bottom 4 small ones. It is 185 minutes, a little more than 3 hours, propagating a distance of vertically 300 km, but 1840.2 km long in space. In addition, the sound speed C is given in the upper right panel, calculated by assuming $T_0 = 288$ °K. It keeps constant at different altitudes due to the isothermal condition. Furthermore, the lower left panel exposes the vertical profiles of the three wavelengths λ_x, λ_y, and λ_z. All of them do not change versus height. Lastly, the lower right panel exposes the three periods which also keep the same in altitudes.

ii. *Quasi-hydrostatic*

If the hydrostatic condition is relaxed to quasi-hydrostatic, that is, the wind components are nonzero ($U \neq 0$ and/or $V \neq 0$) but uniform in space, while keeping other constraints unchanged, Eqs.(15-17) provide

$$\frac{\mathrm{d}x}{\mathrm{d}t} = U - A_{11}k, \ \frac{\mathrm{d}y}{\mathrm{d}t} = V - A_{11}l, \ \frac{\mathrm{d}z}{\mathrm{d}t} = \frac{1}{A_0^*} \tag{22}$$

along with the same coefficients as defined by Eq.(20). Eq.(21) is thus updated as follows:

$$\frac{x}{k - k_s} = \frac{y}{l - l_s} = \frac{z}{m}\left(\frac{\omega_b^2}{\Omega^2} - 1\right), \quad \text{along with } \Omega = \omega - \omega_s \tag{23}$$

Obviously, Eq.(23) is a generalized expression of Eq.(21) to describe straight rays in space but with shifts k_s, l_s, and ω_s in k, l, and ω, respectively:

$$k_s = \frac{U}{A_{11}} = \frac{\Omega^4 - C^2\omega_b^2 k_h^2}{\Omega C^2\left(\Omega^2 - \omega_b^2\right)}U \approx \frac{k_h^2}{\Omega}U, \ l_s = \frac{V}{A_{11}} \approx \frac{k_h^2}{\Omega}V, \ \omega_s = kU + lV \tag{24}$$

Accordingly, regardless of the shifts, rays are still straight lines propagating in space, similar to Fig.1.

b) Hines' locally isothermal and shear-free atmosphere

i. *Hydrostatic*

If the atmosphere is hydrostatic ($U = V = 0$), and T (or C) is constant in time and uniform locally (i.e., $k_T = 0$), the set of ray equations of Hines' model assumes can be obtained from Eqs.(15-17) as follows:

$$\left.\begin{array}{l} \frac{\mathrm{d}x}{\mathrm{d}t} = -A_{11}k,\ \frac{\mathrm{d}y}{\mathrm{d}t} = -A_{11}l,\ \frac{\mathrm{d}z}{\mathrm{d}t} = \frac{1}{A_0^*} \\ \frac{\mathrm{d}k}{\mathrm{d}t} = -A_{22}k_c,\ \frac{\mathrm{d}l}{\mathrm{d}t} = -A_{22}l_c,\ \frac{\mathrm{d}m}{\mathrm{d}t} = -A_{22}m_c \end{array}\right\} \tag{25}$$

where

$$\left.\begin{array}{l} A_0^* = \frac{A_0}{mC^2\Omega^3},\ A_{11} = \frac{\Omega C^2}{A_0}\left(\Omega^2 - \omega_b^2\right),\ A_{22} = \frac{\Omega^3 C^2}{A_0}k_g^2,\ A_0 = \Omega^4 - C^2k_h^2\omega_b^2 \\ k_c = \frac{\partial(\ln C)}{\partial x},\ l_c = \frac{\partial(\ln C)}{\partial y},\ m_c = \frac{\partial(\ln C)}{\partial z} \end{array}\right\} \tag{26}$$

Eq.(**??**) produces a set of ray equations:

$$\frac{\mathrm{d}x}{k} = \frac{\mathrm{d}y}{l} = \left(\frac{\omega_b^2}{\Omega^2} - 1\right)\frac{\mathrm{d}z}{m};\quad \frac{\mathrm{d}k}{k_c} = \frac{\mathrm{d}l}{l_c} = \frac{\mathrm{d}m}{m_c},\quad \text{along with } \Omega = \omega \tag{27}$$

from which we see that in the horizontal x-y plane the projection of the ray trace should be close to a straight line due to the fact that $k_c \sim l_c \ll m_c$, leading to small changes in both k and l, if there are, compared to m.

Fig.2 illustrates the ray features in Hines' locally isothermal and shear-free atmosphere in both forward (in blue) and backward (in red) propagations. The upper left panel displays the 3D traces. Clearly, the rays are no longer straight anymore, in contrast with Fig.1. Impressively, there appear dramatic changes in the range of 85-120 km in altitude. However, as predicted in the above, the projections of the rays in the x-y plane appear straight. The upper right panel shows a distinct difference between the forward and backward rays in the length and time of propagation with the same 300 km height travelled: the forward ray flies away as long as a distance of 700 km in ∼380 min (about 6.5 hours); while the backward one has a journey of 1100 km long in ∼600 min (about 10 hours). The lower two panels expose the vertical profiles of the three wavelengths λ_x, λ_y, & λ_z (left) and the three periods $\tau_a = 2\pi/\omega_a$, $\tau_b = 2\pi/\omega_b$, & $\tau = 2\pi/\Omega$ (right), respectively. Obviously, λ_x and λ_y vary little compared to λ_z; in addition, λ_z is modulated the most between 85 and 120 km altitudes; what is more, τ_a and τ_b have peaks between 85 and 100 km.

To understand the mechanism of these ray features, we plot the mean-field parameters along ray paths in both Fig.3 and Fig.4. The former presents T_0 and C (upper left panel), $\mathrm{d}T_0/\mathrm{d}x$ (upper right panel), $\mathrm{d}T_0/\mathrm{d}y$ (lower left panel), and $\mathrm{d}T_0/\mathrm{d}z$ (lower right panel); and the latter depicts ρ_0 and p_0 (upper left panel), $\mathrm{d}\rho_0/\mathrm{d}x$ (upper right panel), $\mathrm{d}\rho_0/\mathrm{d}y$ (lower left panel), and $\mathrm{d}\rho_0/\mathrm{d}z$ (lower right panel). It is seen that T_0 (or C), rather than ρ_0

Notes

(or p_0), is responsible for the profile of wave periods. More importantly, it is the gradients of T_0, rather than those of ρ_0, that are correlated evidentally with the abnormal features of the ray propagations. Note that the gradients in the horizontal plane ($\mathrm{d}T_0/\mathrm{d}x$ and $\mathrm{d}T_0/\mathrm{d}y$) is 2 or 3 orders smaller than that in the vertical direction ($\mathrm{d}T_0/\mathrm{d}z$). Thus, the vertical gradient in temperature dominates the modulation.

Notes

Fig.5 draws the altitude profiles of the WKB δ parameter in the forward and backward propagations. The parameter is lower on average in the former case than in the latter case. In either case, it is smaller than 1. Interestingly, in the 85-120 km altitudes, The magnitude becomes apparently higher than that in other altitudes.

ii. *Quasi-hydrostatic*

If the hydrostatic condition is relaxed to quasi-hydrostatic, that is, the wind components are nonzero ($U \neq 0$ and/or $V \neq 0$) but uniform in space, while keeping other constraints unchanged, Eqs.(15-17) provide

$$\left.\begin{array}{l} \frac{\mathrm{d}x}{\mathrm{d}t} = U - A_{11}k,\ \frac{\mathrm{d}y}{\mathrm{d}t} = V - A_{11}l,\ \frac{\mathrm{d}z}{\mathrm{d}t} = \frac{1}{A_0^*} \\ \frac{\mathrm{d}k}{\mathrm{d}t} = -A_{22}k_c,\ \frac{\mathrm{d}l}{\mathrm{d}t} = -A_{22}l_c,\ \frac{\mathrm{d}m}{\mathrm{d}t} = -A_{22}m_c \end{array}\right\} \tag{28}$$

where the coefficients are those expressed in Eq.(**??**). This set of equations updates Eq.(**??**) as follows:

$$\frac{\mathrm{d}x}{k-k_s} = \frac{\mathrm{d}y}{l-l_s} = \left(\frac{\omega_b^2}{\Omega^2} - 1\right)\frac{\mathrm{d}z}{m};\quad \frac{\mathrm{d}k}{k_c} = \frac{\mathrm{d}l}{l_c} = \frac{\mathrm{d}m}{m_c},\quad \text{along with } \Omega = \omega - \omega_s \tag{29}$$

in which shifts k_s, l_s, and ω_s in k, l, and ω, respectively, are already given in Eq.(24). Accordingly, regardless of the shifts, the profiles of rays are similar to Figs.2∼4 in this quasi-static case.

c) Nonisothermal and shear-free atmosphere

Realistic atmosphere is nonisothermal, i.e., $k_T \neq 0$. We therefore extend Hines' locally isothermal model for more generalized situation where ω_a and ω_b are substituted by ω_A and ω_B, respectively. To save space, we just take the hydrostatic case ($U = V = 0$) as an example. In this case, Eqs.(15-17) provide

$$\left.\begin{array}{l} \frac{\mathrm{d}x}{\mathrm{d}t} = -A_{11}k,\ \frac{\mathrm{d}y}{\mathrm{d}t} = -A_{11}l,\ \frac{\mathrm{d}z}{\mathrm{d}t} = \frac{1}{A_0^*} \\ \frac{\mathrm{d}k}{\mathrm{d}t} = -A_{22}k_c,\ \frac{\mathrm{d}l}{\mathrm{d}t} = -A_{22}l_c,\ \frac{\mathrm{d}m}{\mathrm{d}t} = -A_{22}m_c \end{array}\right\} \tag{30}$$

where

$$\left.\begin{array}{l} A_0^* = \frac{A_0}{mC^2\Omega^3},\ A_{11} = \frac{\Omega C^2}{A_0}\left(\Omega^2 - \omega_B^2\right),\ A_{22} = \frac{\Omega^3 C^2}{A_0}k_g^2,\ A_0 = \Omega^4 - C^2k_h^2\omega_B^2 \\ k_c = \frac{\partial(\ln C)}{\partial x},\ l_c = \frac{\partial(\ln C)}{\partial y},\ m_c = \frac{\partial(\ln C)}{\partial z} \end{array}\right\} \tag{31}$$

Eq.(30) produces a set of ray equations:

$$\frac{\mathrm{d}x}{k}=\frac{\mathrm{d}y}{l}=\left(\frac{\omega_B^2}{\Omega^2}-1\right)\frac{\mathrm{d}z}{m};\quad \frac{\mathrm{d}k}{k_c}=\frac{\mathrm{d}l}{l_c}=\frac{\mathrm{d}m}{m_c},\quad \text{along with } \Omega=\omega \tag{32}$$

Eqs.(30∼32) are similar to Eqs.(25∼27), respectively. Thus, the ray features in the present nonisothermal case are basically the same as Hines' locally isothermal case. For example, in the horizontal x-y plane the projection of the ray trace is straight approximately due to the fact that $k_c \sim l_c \ll m_c$ and thus k and l are nearly constant compared to m. As introduced in the last subsection, ray features are dominantly influenced by the mean-field temperature and its spatial gradients. Fig.6 presents the characteristics of ray propagation: the 3D ray traces in the upper left panel; the ray distances versus time in the upper right panel; the three wavelengths λ_x, λ_y, & λ_z in the lower left panel, and the three periods $\tau_A = 2\pi/\omega_A$, $\tau_B = 2\pi/\omega_B$, and $\tau = 2\pi/\Omega$ in the lower right panel. Fig.7 displays the altitude profiles of mean-field T_0 and C (upper left), $\mathrm{d}T_0/\mathrm{d}x$ (upper right), $\mathrm{d}T_0/\mathrm{d}y$ (lower left), and $\mathrm{d}T_0/\mathrm{d}z$ (lower right), respectively.

Comparing Hines' model (Figs.2 & 3) with the nonisothermal model (Figs.6 & 7) reveals that the introduction of the new ingredient, k_T, in the cut-off and buoyancy periods results in (1) mitigated bulges of the two ray traces in the 85-120 km altitude; (2) lower speeds of ray propagation in space, e.g., Hines' model gives an average of 1.8 km/min (about 1100 km in 600 minutes), while the nonisothermal model shows 1.3 km/min (1050 km in 800 minutes) in the backward case. However, it is subtle to discern its effects on the profiles of wavelengths, periods, temperature (or, equivalently, sound speed), as well as the temperature gradients.

d) Fully isothermal and wind-shearing atmosphere

In this case, $k_T = 0$, but $\mathbf{v}_0 \neq 0$, $\partial\mathbf{v}_0/\partial t \neq 0$, and $\partial\mathbf{v}_0/\partial\mathbf{r} \neq 0$. Eqs.(15-17) yield

$$\left.\begin{aligned}&\tfrac{\mathrm{d}t}{\mathrm{d}z}=A_0,\ \tfrac{\mathrm{d}x}{\mathrm{d}z}=A_0\left(U-A_{11}k+A_{12}\tfrac{\partial U}{\partial z}\right),\ \tfrac{\mathrm{d}y}{\mathrm{d}z}=A_0\left(V-A_{11}l+A_{12}\tfrac{\partial V}{\partial z}\right)\\&\tfrac{\mathrm{d}k}{\mathrm{d}z}=-A_0\Delta_x,\ \tfrac{\mathrm{d}l}{\mathrm{d}z}=-A_0\Delta_y,\ \tfrac{\mathrm{d}m}{\mathrm{d}z}=-A_0\Delta_z,\ \tfrac{\mathrm{d}\Omega}{\mathrm{d}z}=-A_0A_{21}\Delta_t\end{aligned}\right\} \tag{33}$$

where

$$\left.\begin{aligned}&\Delta_x=k\tfrac{\partial U}{\partial x}+l\tfrac{\partial V}{\partial x},\ \Delta_y=k\tfrac{\partial U}{\partial y}+l\tfrac{\partial V}{\partial y},\ \Delta_z=k\tfrac{\partial U}{\partial z}+l\tfrac{\partial V}{\partial z},\ \Delta_t=k\tfrac{\partial U}{\partial t}+l\tfrac{\partial V}{\partial t}\\&A_0=\tfrac{A_{00}}{mC^2\Omega^3},\ A_{11}=\tfrac{\Omega C^2\left(\Omega^2-\omega_b^2\right)}{A_{00}},\ A_{12}=\tfrac{\eta\Omega^3C^2/\Delta_z}{A_{00}},\ A_{21}=\tfrac{\Omega^4-C^2k_h^2\omega_b^2}{A_{00}}\end{aligned}\right\} \tag{34}$$

in which $A_{00}=\Omega^4-C^2(\omega_b^2k_h^2+\eta\Omega^2)$ and $\eta=(1-\gamma/2)\,g\Delta_z/(2\Omega C^2)-\Delta_z^2/(4\Omega^2)$.

Under the isothermal condition, Figs.8∼11 display the heavy impacts of wind shears on the characteristics of ray propagation. In Fig.8, the upper left panel is the 3D ray traces. Both the forward and backward rays are wriggling through the 3D space by following two different paths. The difference is obviously shown in the upper right panel: the forward ray (in blue) travels ∼530 km in about 380 minutes between the sea level and the 300 km altitude, while the backward ray (in red) hikes around 750 km in about 320 minutes. The

Notes

lower two panels of the figure present the wave lengths and intrinsic wave periods of the propagation, respectively. In the LHS panel, λ_y appears constant in altitude, relatively speaking, and does λ_z except the heights of 100-150 km. The altitude dependance of λ_x in the LHS panel is similar to that of τ in the RHS panel: (1) below 80 km altitude they keep roughly unchanged. (2) λ_x and τ stabilize with their respective minimum values in 120-135 km altitude in the forward propagation, while with maximum values in 130-145 km altitude in the backward propagation. The two arrow lines label these values. (3) above 200 km altitude, the forward parameters increase monotonously and the backward ones do not change anymore.

Along ray paths the altitude profiles of the mean-field zonal wind U and meridional wind V are described in the upper left and upper right panels in Fig.9, respectively. The WKB δ parameter is given in the lower panel. Below 80 km altitude and above 200 km altitude both U and V are either unchanging or vary quasi-linearly. On the contrary, between the two altitudes, they exhibit oscillatory features with both positive and negative speeds. As far as δ, most of its amplitudes are smaller than 1, while in 100-150 km altitudes there are a couple of peaks for both forward and backward situations, respectively. Between the peaks of each pair, there exists zero-δ heights of 120-135 km in the forward case and of 130-145 km in the backward case. The two zero-δ slots correspond to the two zones of the minimum λ_x and τ values, respectively, in the lower two panels of Fig.8. Note that δ can be as high as 8, which is larger than 1, for regular ray propagation as exposed in the upper left panel of Fig.8.

The altitude profiles of the mean-field wind gradients in temporal coordinate t and spatial ones (x, y, z) are illustrated in Figs.10 and Fig.11. The gradients in U and V have following characteristics: (1) The magnitude of all the U-gradients is larger than that of the V-gradients, particularly below 50 km altitude where the V-gradients are nearly zero. (2) While $\mathrm{d}(U,V)/\mathrm{d}t \sim$ several m/s per hour in magnitude, $\mathrm{d}(U,V)/\mathrm{d}x \sim \mathrm{d}(U,V)/\mathrm{d}y \ll \mathrm{d}(U,V)/\mathrm{d}z \sim$ several m/s per km in magnitude. This indicates that it is the wind shears (horizontal wind velocity gradients in altitude), rather than its gradients in the horizontal plane, that play the dominant role to influence wave propagation in atmosphere. (3) Below 80 km and above 200 km altitudes, all the wind gradients are smaller than that between the two altitudes. This reminds us that the effects of the wind gradients on wave propagation cannot not be omitted, especially in the middle atmosphere.

e) Nonisothermal and wind-shearing atmosphere: Generalized formulation

To adopt $k_T \neq 0$ by relaxing the constraint of $k_T = 0$ in the above Subsection, Eqs.(15-17) gives rise to the most generalized set of ray-tracing equations as follows:

$$\left.\begin{aligned} &\frac{\mathrm{d}t}{\mathrm{d}z} = A_0,\ \frac{\mathrm{d}x}{\mathrm{d}z} = A_0\left(U - A_{11}k + A_{12}\frac{\partial U}{\partial z}\right),\ \frac{\mathrm{d}y}{\mathrm{d}z} = A_0\left(V - A_{11}l + A_{12}\frac{\partial V}{\partial z}\right) \\ &\frac{\mathrm{d}k}{\mathrm{d}z} = -A_0\left(\Delta_x + A_{22}C_x\right),\ \frac{\mathrm{d}l}{\mathrm{d}z} = -A_0\left(\Delta_y + A_{22}C_y\right),\ \frac{\mathrm{d}m}{\mathrm{d}z} = -A_0\left(\Delta_z + A_{22}C_z\right) \\ &\frac{\mathrm{d}\Omega}{\mathrm{d}z} = -A_0\left(A_{21}\Delta_t - A_{22}C_t\right) \end{aligned}\right\} \quad (35)$$

where $\Delta_{x,y,z,t}$ are expressed in Eq.(34), and,

$$\left.\begin{array}{l} C_x = \frac{1}{C}\frac{\partial C}{\partial x},\ C_y = \frac{1}{C}\frac{\partial C}{\partial y},\ C_z = \frac{1}{C}\frac{\partial C}{\partial z},\ C_t = \frac{1}{C}\frac{\partial C}{\partial t}; \\ A_0 = \frac{A_{00}}{mC^2\Omega^3},\ A_{11} = \frac{\Omega C^2\left(\Omega^2-\omega_B^2\right)}{A_{00}},\ A_{12} = \frac{\eta\Omega^3C^2/\Delta_z}{A_{00}}, \\ A_{21} = \frac{\Omega^4-C^2k_h^2\omega_B^2}{A_{00}},\ A_{22} = \frac{\Omega^3(\omega_A^2-C^2K^2-\frac{\Delta_z^2C^2}{4\Omega^2})}{A_{00}} \end{array}\right\} \quad (36)$$

in which $A_{00} = \Omega^4 - C^2(\omega_B^2k_h^2 + \eta\Omega^2)$ and η keeps the same as that attached to Eq.(34).

In addition to the effects of the mean-field wind, this generalized case takes into consideration the influences of altitude-dependent temperature, as well as the density (and thus the pressure), and their gradients in time and space on the ray propagation. Figs.12∼17 illustrate the results. In comparison with that of Fig.8, the upper left panel of Fig.12 exhibits a less wriggling feature in both forward and backward propagations. The upper right panel shows that, while the forward ray (in blue) passes ∼400 km in about 250 minutes between the sea level and the 300 km altitude, the backward one (in red) spends about 380 minutes to fly back to the sea level after a ∼800 km journey. The speed of the former (400/250≈1.6 km/min) is higher than that in Fig.8 (530/380≈1.4 km/min), while the speed of the latter (800/380≈2.1 km/min) is approximately the same as that in Fig.8 (750/320≈2.3 km/min). In addition, the altitude profiles of both the three wavelengths (lower left panel) and the intrinsic wave period (lower right panel) demonstrate that below 150 km nonisothermality results in stronger fluctuations in comparison with Fig.8, especially lower than 100 km altitude. Interestingly, the forward wave period is shorter than the backward one in Fig.12 at most altitudes, in contrast to the fact that it is always longer than that in Fig.8.

In Fig.13, the upper panel portrays the altitude profiles along ray paths of WKB δ. The parameter is smaller than 0.2 above 160 km altitude. Below the altitude, the forward δ is larger than the backward one between 130 km and 160 km; but it always is smaller below 130 km. This is different from the results given in Fig.9, where the the forward δ is usually larger than the backward one, particularly in the 100-150 km altitude. With respect to the mean-field zonal wind (lower left panel) and the meridional wind (lower right panel), the profiles in Fig.13 are similar to those in Fig.9.

Figs.14 & 15 draw the altitude profiles of density gradients (LHS panels) and temperature gradients (RHS panels) in t, x, y, and z. Except the t-related ones, these structures reproduce those presented in Figs.3 & 4, respectively, with the same order of magnitudes. For $\mathrm{d}\rho_0/\mathrm{d}t$ and $\mathrm{d}T_0/\mathrm{d}t$, their appearances follow the patterns of their respective families, but with different units of each. In addition, Figs.16 & 17 delineate the altitude profiles of zonal wind gradients (LHS panels) and meridional ones (RHS panels) in t, x, y, and z. The figures do not disclose discernable changes from those given in 10 & 11, respectively.

f) Nonisothermal and wind-shearing atmosphere: Influence of initial wavelengths

In the above Subsections, we arbitrarily selected the same group of initial horizontal wavelengths, $\lambda_{x0} = 350$ km and $\lambda_{y0} = 50$ km, to exhibit the features of the ray propagation under different acoustic-gravity wave modes. In this Subsection, we choose several groups of initial horizontal wavelengths to exhibit the influence of the parameter on the ray propagation (taking the forward situation as an example) in the generalized nonisothermal and shearing mode. The considered wavelengths include following two groups of pairs: (1) $\{\lambda_{x0}, \lambda_{y0}\} = \{2\pi\times350, 2\pi\times50\}$, $\{2\pi\times350, -2\pi\times50\}$, $\{-2\pi\times350, 2\pi\times50\}$,

$\{-2\pi \times 350, -2\pi \times 50\}$; and (2) $\{\lambda_{x0}, \lambda_{y0}\} = \{2\pi \times 50, 2\pi \times 350\}$, $\{2\pi \times 50, -2\pi \times 350\}$, $\{-2\pi \times 50, 2\pi \times 350\}$, $\{-2\pi \times 50, -2\pi \times 350\}$, where the unit of all the parameters are in km, and the negative values represent the propagating direction of the related wave components is in the reverse direction of the coordinate in the frame of reference. In the simulation, the initial extrinsic wave period ω keeps unchanged at 30 minutes.

Notes

Fig.18 demonstrates the ray paths in space with these two groups of initial wavelengths. In each group, the four cases are discriminated by four different colors (black, blue, red, and green), respectively. Several distinct features of the ray propagation are exposed by both the upper and lower panels of the figure: (1) All the rays propagate in space along non-straight paths in a quadrant determined by, and opposite to, the initial wave vectors, respectively, in the horizontal plane, $\{k_0 = 2\pi/\lambda_{x0}, l_0 = 2\pi/\lambda_{x0}\}$. For example, in the two panels, the ray in black ($\lambda_{x0} > 0$ and $\lambda_{y0} > 0$) is oriented to evolve in the third quadrant ($x < 0$ and $y < 0$); similarly, the ray in blue ($\lambda_{x0} > 0$ and $\lambda_{y0} < 0$) is in the second quadrant ($x < 0$ and $y > 0$). (2) In the horizontal plane, the ratio between the x-displacement, Δx, and the y-displacement, Δy, of any projected ray paths is in the same order of that of the corresponding wavenumbers. For instance, the ray in red in the upper panel has a ratio of $\Delta x/\Delta y \approx 45/270 = 0.16$ while the wavenumber ratio is $k_0/l_0 = 0.14$; also, the ray in black in the lower panel has a ratio of $\Delta x/\Delta y \approx 320/40 = 8$ while the wavenumber ratio is $k_0/l_0 = 7$. (3) Between 80 km and 150 km altitude all rays experience the most serious modulations. According to the analysis in the previous Subsections, these influences are exerted dominantly by the mean-field wind components and their shears. (4) By comparison with the upper left panel of Fig.12, these modulations caused by the wind components and their shears become mitigated if the horizontal wavelengths are longer, as shown in the upper panel of Fig.18.

Fig.19 portrays the temporal features of both the ray length (thick lines) and the vertical increments (thin lines) in the above two groups of the wave propagations. All the ray paths are approximately proportional to time, with a propagation speed of 15∼18 km/min in space: the upper panel gives 400/23≈17 km/min (black), 400/26≈15 km/min (blue), 400/27≈15 km/min (red), and 400/25=16 km/min (green); and the lower panel presents 450/32≈14 (black), 400/22≈18 km/min (blue), 360/20=18 km/min (red), and 400/25=16 km/min (green). Relatively, the vertical propagation speed is lower, around 9∼15 km/min, if assuming a linear relation between the height and time. These speeds are much higher than those obtained from the upper right panel of Fig.12: it is merely no more than 2 km/min for the four traces. Thus, rays with longer initial horizontal wavelengths travel faster. In fact, all the rays in Fig.19 reach heights of 300-400 km in only no more than 30 minutes; by contrast, those in Fig.12 arrive 300-800 km altitudes after more than 260 minutes.

Fig.20 displays the development of the wavelengths λ_x (upper left panel), λ_y (upper right panel), λ_z (lower left panel), and the intrinsic wave period τ (lower right panel) along the ray paths in the two groups of wave propagations. The most conspicuous feature stays in the modulations of the four parameters below 200 km altitude, particularly at the height of 100-150 km. By checking Fig.19 we know this corresponds to 80-120 km altitude, the most extreme changing region of both the mean-field temperature (Fig.7,14,15) and zonal & meridional winds (Fig.13,16,17). Besides, for the horizontal wavelength (λ_x or λ_y; the upper two panels in the two groups), its magnitude becomes higher than the initial value

(λ_{x0} or λ_{y0}) if the value is positive, i.e., the initial wave vector component is in the x (or y) direction. For example, in the upper right panel in the first group, the red curve denotes the case of $\lambda_{y0} = 2\pi \times 50 > 0$ km. Along the ray, λ_y increases and peaks at 150 km distance along the ray with 51.2 km. By contrast, if λ_{x0} (or λ_{y0}) is negative, i.e., the initial wave vector component is opposite to the x (or y) direction, the magnitude of λ_x (or λ_y) decreases. See the green curve in the upper right panel in the second group. In this case, $\lambda_{y0} = -2\pi \times 350 < 0$ km. Along the ray, $\mid \lambda_y \mid$ decreases to 300 km at about 100 km distance along the ray.

However, the vertical wavelength, λ_z, behaves differently as exhibited by the two lower left panels in the two groups. Irrelevant to the directions of initial horizontal wavevectors, the upward propagating waves have negative λ_z. Its magnitude starts at $\lambda_{z0} = 2\pi \times 12$ km. After a surprising drop of $\lambda_z/(2\pi)$ to below 8 km in within 20 km ray path, it undergoes a large swing between 3 and 8 km in the first group, and between 3 and 11 km in the second group, before stabilizing at 3-5 km and 3-9.5 km, respectively, after a journey of 300 km long in the ray propagation. These final values correspond to $\lambda_z \sim$ 20-60 km. Impressively, the wave period τ has a similar trend as shown in the two lower right panels of the two groups: it decreases sharply at first, then goes up and down, and recovers finally to stabilize at a period which diverge only within 1 minute (the first group) and 2 minutes (the second group) from the initial values, respectively. Because the initial perod is 30 minutes, we may neglect this divergence in dealing with measurements, that is, the wave period can be assumed constant in wave propagations.

IV. Summary and Discussion

Since the 1960s, the influence of mean-field properties (such as zonal and meridional winds, background temperature) on the propagation of atmospheric acoustic-gravity waves has become one of the important topics in space physics. The related ray-tracing technique has also been developed to investigate gravity wave propagation under the effects of background wind and temperature variations. Due to the importance of an accurate description of mean-field properties and their effects in the clarification of the observed wave-driven phenomena in atmosphere (e.g., *Hickey et al.* 1998), we first of all took into account the wind-shearing and nonisothermal effects, as well as the Coriolis effect, to extend Hines' locally isothermal and shear-free model to describe the modes of generalized inertio-acoustic-gravity waves under different situations below 200 km altitude, where all dissipative terms (such as viscosity and heat conductivity) were neglected (*Ma et al.* 2014). The obtained dispersion relation recovers all the known atmospheric wave modes.

In this paper, we used the generalized dispersion relation to investigate the effects of the wind shears and nonisothermality on the ray propagation of acoustic-gravity waves. The derived general set of ray equations not only reproduces ME95's derivations under Hines' locally isothermal and shear-free conditions, but also provides the equation to describe the time-dependent variation of the intrinsic wave frequency. Our ray-tracing simulations accommodate five different types of atmospheric models, starting from the simplest situation to the most complicated one: (1) fully isothermal, and shear-free atmosphere under both hydrostatic and quasi-hydrostatic conditions; (2) Hines' locally isothermal and shear-free atmosphere under both hydrostatic and quasi-hydrostatic conditions; (3) nonisothermal and shear-free atmosphere under hydrostatic conditions; (4) fully isothermal and wind-shearing atmosphere; (5) nonisothermal and wind-shearing atmosphere (generalized formulation; influence of initial wavelengths). In every step, a set of ray equations was derived to numerically code into a global ray-tracing model and calculate the profiles of ray traces in space and time; that of the wavelengths and intrinsic wave periods along

Notes

the ray paths; that of the mean-field density, pressure, or temperature and the horizontal winds, as well as their gradients if available; and that of the WKB criterion parameter, δ in a few typical cases.

Our studies demonstrated the influences of wind shears and atmospheric nonisothermality on the ray propagation. In an isothermal and shear-free atmosphere, ray paths follow straight lines in space and time; both forward and backward-mapping traces are superimposed upon each other; wavelengths ($\lambda_{x,y,z}$), as well as the intrinsic wave period (τ), keep constant versus altitude. If Hines' locally isothermal condition is applied, i.e., including the effect of the altitude-dependent temperature, rays become non-straight spatially, but their projections in the horizontal plane keep straight. In this case, the forward and backward rays are no longer overlain, and $\lambda_{x,y,z}$ give discernable changes but τ does not change. All the obvious variations happen in 80-150 km altitude. If the temperature constraint is relaxed to the nonisothermal condition by adding the effect of temperature gradients in x, y, z and t, the results do not exhibit perceptible difference. In the presence of wind shears, as well as zonal and meridional wind gradients in space and time, but the atmosphere keeps isothermal, ray paths are violently modulated, particularly at 80-150 km altitude where $\lambda_{x,y,z}$ and τ exhibit striking variations. More importantly, the forward rays and the backward ones never propagate along the same paths. If the nonisothermal condition is employed by considering the effects of temperature variations in x, y, z and t, the modulations at 0-80 km altitude also become obvious. As far as the WKB δ parameter, though it is smaller than 0.4 in Hines' locally isothermal model, in agreement with ME95's estimation, it can be driven to close to 3 by the wind shears and nonisothermality. Lastly, we found that longer initial horizontal wavelengths bring about mitigated modulations to ray paths and faster speeds in ray propagation.

We stress that ME95's ray-tracing model is based on the dispersion relation derived from Hines locally isothermal and shear-free model. By contrast, our study expends ME95's formulation to obtain a generalized set of ray-tracing equations by taking into account the effects of wind shears and atmospheric nonisothermality on the ray propagation. The focus of this paper is to illustrate the influences of the effects on acoustic-gravity waves travelling from sea level to 200 km altitude within which the dissipation terms can be reasonably neglected. We therefore pay attention dominantly to the waves which are able to penetrate atmosphere and reach the ionospheric height above 80 km altitude, with little energy attenuation, and ignore those waves which are either reflected or in the cut-off region (for details of the wave features in these two cases see, e.g., *Ding et al.* 2003). Naturally, we avoid to consider such terms related to, e.g., WKB violation, wave saturation or damping, energy attenuation or intensification, dynamical and convective instabilities, which are of little relevance to our study. Instead, we concentrate on the waves which are capable of survival from every damping process during their propagations upward from the sea level to some observational heights. Thus, the result shown in this paper are suitable to provide a reference for data-fit modeling studies with measurements in space, e.g., mesosphere and/or troposphere, where information of the background wind and temperature profiles are available, owing to the fact that the close relationship between the ray paths and the mean-field atmospheric properties can be demonstrated more evidently than before via the approach provided in the text.

V. Acknowledgments

The Fortran code and simulation data in this paper are available on request to John.

References Références Referencias

1. AGARD (1972), Effects of Atmospheric Acoustic Gravity Waves on Electromagnetic Wave Propagation, *Conf. Proc., 115*, Harford House, London.
2. Beer, T. (1974), Atmospheric Waves, John Wiley, New York.
3. Bertin, F., J. Testud, and L. Kersley (1975), Medium scale gravity waves in the ionospheric F-region and their possible origin in weather disturbances, *Planet. Space Sci.*, 23, 493-507.
4. Bolt, B. A. (1964), Seismic air waves from the great 1964 Alaska earthquake, *Nature, 202*, 1095-1096.
5. Broutman, D., and S. D. Eckermann (2012), Analysis of a ray-tracing model for gravity waves generated by tropospheric convection, *J. Geophys. Res., 117*, D05132, doi:10.1029/2011 JD016975.
6. Bruce, C. H., D. W. Peaceman, H. H. Rachford, and J. P. Rice (1953), Calculations of unsteady-state gas flow through porous media, *J. Petrol. Tech.*, 5, 79-92.
7. Brunt, D. (1927), The period of simple vertical oscillations in the atmosphere, *Quart. J. Royal Meteor. Soc.*, 53, 30-32.
8. Calais, E., J. B. Minster, M. A. Hofton, and M. A. H. Gedlin (1998), Ionospheric signature of surface mine blasts from global positioning system measurements, *Geophys. J. Int., 132*, 191-202.
9. Cole, J. D., and C. Greifinger (1969), Acoustic-gravity waves from an energy source at the ground in an isothermal atmosphere, *J. Geophys. Res., 74*, 3693-3703.
10. Cowling, D. H., H. D. Webb, and K. C. Yeh (1971), Group rays of internal gravity waves in a wind-stratified atmosphere, *J. Geophys. Res., 76*, 213-220.
11. DeMajistre, R., L. J. Paxton, and D. Bilitza (2007), Comparison of ionospheric measurements made by digisondes with those inferred from ultraviolet airglow, *Adv. Space Res., 39,* 918-925.
12. Ding, F., W. X. Wan, and H. Yuan (2003), The influence of background winds and attenuation on the propagation of atmospheric gravity waves, *J. Atmos. and Solar-Terr. Phys., 65*, 857-869.
13. Dutton, J. A. (1986), The Ceaseless Wind, Dover, New York.
14. Eckart, C. (1960), Hydrodynamics of oceans and atmospheres, Pergamon, New York.
15. Eckermann, S. D. (1997), Influence of wave propagation on the Doppler spreading of atmospheric gravity waves, *J. Atmos. Sci., 54*, 2554-2573.
16. Einaudi, F. and Hines, C. O. (1970), WKB approximation in application to acousticgravity waves, *Can. J. Phys., 48*, 14581471.
17. Fovell, R., D. Durran, J. R. Holton (1992), Numerical simulations of convectively generated stratospheric gravity waves. *J. Atmos. Sci., 49*, 1427-.
18. Francis, S. H. (1973), Acoustic-gravity modes and large-scale traveling ionospheric disturbances of a realistic, dissipative atmosphere, *J. Geophys. Res., 78*, 2278-2301.
19. Francis, S. H. (1974), A theory of medium-scale traveling ionospheric disturbances, *J. Geophys. Res., 79*, 5245-5260.
20. Francis, S. H. (1975), Global propagation of atmospheric gravity waves: a review. *J. Atmos. Terr. Phys., 37*, 10111030, IN9, 10311054.
21. Franke, S. J., X. Chu, A. Z. Liu, and W. K. Hocking (2005), Comparison of meteor radar and Na Doppler lidar measurements of winds in the mesopause region above Maui, HI, *J. Geophys. Res., 110*, D09S02, doi:10.1029/2003JD004486.
22. Fritts, D. C. (1984), Gravity wave saturation in the middle atmosphere: A review of theory and observations, *Rev. Geophys. Space Phys., 22*, 275-308.

Notes

Notes

23. Fritts, D. C. (1989), A review of gravity wave saturation processes, effects, and variability in the middle atmosphere, *Pure Appl. Geophys., 130*, 343-371.
24. Fritts, D. C., and M. J. Alexander (2003), Gravity wave dynamics and effects in the middle atmosphere, *Rev. Geophys., 41*, 1003, doi:10.1029/2001RG000106.
25. Fritts, D. C., and T. S. Lund (2011), Gravity wave influences in the thermosphere and ionosphere: Observations and recent modeling, in: *Aeronomy of the Earths Atmosphere and Ionosphere*, ed.: Abdu, M. A., Pancheva, D., and Bhattacharyya, A., Springer, 109-130.
26. Fritts, D. C., B. P. Williams, C. Y. She, J. D. Vance, M. Rapp, F.-J. LΥubken, A. Mullemann, F. J. Schmidlin, and R. A. Goldberg (2004), Observations of extreme temperature and wind gradients near the summer mesopause during the MaCWAVE/MIDAS rocket campaign, *Geophys. Res. Lett., 31*, L24S06, doi:10.1029/2003GL019389.
27. Georges, T. M. (1968), Acoustic-gravity waves in the atmosphere, Symposium Proceedings, U .S. Government Printing Office, Washinton, D. C.
28. Gershman, B. N., and G. I. Grigor'ev (1968), Traveling ionospheric disturbances–A review, *Izv. Vyssh. Ucheb. Zaved. Radiofizika* (Engl. Transl.), 11, 5-27.
29. Ghodpage, R. N., A. Taori, P. T. Patil, S. Gurubaran, A. K. Sharma, S. Nikte, and D. Nade (2014), Airglow measurements of gravity wave propagation and damping over Kolhapur (16.5◦N, 74.2◦E), Intern. *J. Geophys., 2014*, ID514937, 1-9.
30. Gill, A. E. (1982), Atmosphere-ocean dynamics. Academic Press, Orlando, FL, International Geophysics Series.
31. Gossard, E. E., and W. H. Munk (1954), On gravity waves in the atmosphere, *J. Meteorol., 11*, 259-269.
32. Grigorev, G. I. (1999), Acoustic-gravity waves in the Earth's atmosphere (review). *Radio- phys. Quant. Electron., 42*, 3-25.
33. Hall, C. M., T. Aso, and M. Tsutsumi (2007), Atmospheric stability at 90 km, 78°N, 16°E, *Earth Planets Space, 59*, 157-164.
34. Harkrider, D. G. (1964), Theoretical and observed acoustic-gravity waves from explosive sources in the atmosphere, *J. Geophys. Res.*, 69, 5295-5321.
35. Harris, I. and W. Priester (1962), Time dependent structure of the upper atmosphere, *J. Atmos. Sci.*, 19, 286-301.
36. Hedin, A. E. (1991), Extension of the MSIS thermosphere model into the middle and lower atmosphere, *J. Geophys. Res., 96*, 11591172.
37. Hedin, A. E., M. A. Biondi, R. G. Burnside, G. Hernandez, R. M. Johnson, T. L. Killeen, C. Mazaudier, J. W. Meriwether, J. E. Salah, R. J. Sica, R. W. Smith, N. W. Spencer, V. B. Wickwar, T. S. Virdi (1991). Revised global model of thermosphere winds using satellite and ground-based observations. *J. Geophys. Res., 96*, 7657-7688.
38. Hedin, A. E., E. L. Fleming, A. H. Manson, F. J. Schmidlin, S. K. Avery, R. R. Clark, S. J. Franke, G. J. Fraser, T. Tsuda, F. Vial, and R. A. Vincent (1996), Empirical wind model for the upper, middle and lower atmosphere, *J. Atmos. Terr. Phys*. 58, 1421-1447.
39. Heisler, L. H. (1958), Anomalies in ionosonde records due to travelling ionospheric disturbances, *Aust. J. Phys., 11*, 79-90.
40. Hickey M. P., and K. D. Cole (1987), A quantic dispersion equation for internal gravity waves in the thermosphere, *J. Atmos. Terr. Phys., 49*, 889-899.

41. Hickey M. P., and K. D. Cole (1988), A numerical model for gravity wave dissipation in the thermosphere, *J. Atmos. Terr. Phys., 50*, 689-697.
42. Hickey, M. P., Richard L. Walterscheid, Michael J. Taylor, William Ward, Gerald Schubert, Qihou Zhou, Francisco Garcia, Michael C. Kelly, and G. G. Shepherd (1997), Numerical simulations of gravity waves imaged over Arecibo during the 10-day January 1993 campaign, *J. Geophys. Res., 102*, 11,475-11,489.
43. Hickey, M. P., M. J. Taylor, C. S. Gardner, and C. R. Gibbons (1998). Full-wave modeling of small-scale gravity waves using Airborne Lidar and Observations of the Hawaiian Airglow (ALOHA-93) O(^{1}S) images and coincident Na wind/temperature lidar measurements. *J. Geophys. Res., 103*, 6439-6453.
44. Hickey, M. P., R. L. Walterscheid, and G. Schubert (2000), Gravity wave heating and cooling in Jupiters thermosphere, *Icarus, 148*, 266–281.
45. Hickey, M. P., G. Schubert, and R. L. Walterscheid (2001), Acoustic wave heating of the thermosphere, *J. Geophys. Res., 106*, 21,543-21,548.
46. Hickey, M. P., G. Schubert, and R. L. Walterscheid (2009), Propagation of tsunami-driven gravity waves into the thermosphere and ionosphere, *J. Geophys. Res., 114*, A08304, doi:10.1029/2009JA014105
47. Hines, C. O. (1960), Internal atmospheric gravity waves at ionospheric heights, *Can. J. Phys., 38*, 1441-1481.
48. Hines, C. O. (1963), The upper atmosphere in motion. *Q.J.R. Meteorol. Soc.*, 89, 1-42.
49. Hines, C. O. (1967), On the nature of traveling ionospheric disturbances launched by the low-altitude nuclear explosions, *J. Geophys. Res., 72*, 1877-1882.
50. Hines, C. O. (1971), Generalization of the Richardson criterion for the onset of atmospheric turbulence, *Q. J. R. Met Soc., 97*, 429-439.
51. Hines, C. O. (1972), Gravity waves in the atmosphere, *Nature, 239*, 73-78.
52. Hines, C. O. (1974) WKB Approximation in Application to Acoustic-Gravity Waves, in: *The Upper Atmosphere in Motion*, American Geophysical Union, Washington, D. C., 508-530.
53. Hines, C. O., and D.W. Tarasick (1987), On the detection and utilization of gravity waves in airglow studies, *Planet. Space Sci.*, 35, 851-866.
54. Hocke, K., and K. Schlegel (1996), A review of atmospheric gravity waves and travelling ionospheric disturbances: 1982-1995, *Ann. Geophys.*, 14, 917-940.
55. Holton, J. R. (1992), An Introduction to Dynamic Meteorology. Academic Press, San Diego.
56. Hooke, W. H. (1968), Ionospheric irregularities produced by internal atmospheric gravity waves, *J. Atmosph. Sol.-Terr. Phys., 30*, 795-823.
57. Huang, Y. N., K. Cheng, and S. W. Chen (1985), On the detection of acoustic-gravity waves generated by typhoon by use of real time HF Doppler frequency shift sounding system, *Radio Sci., 20*, 897-906.
58. Igarashi, K., S. Kainuma, I. Nishmuta, S. Okamoto, H. Kuroiwa, T. Tanaka, T. Ogawa (1994), Ionospheric and atmospheric disturbances around Japan caused by the eruption of Mount Pinatubo on June 15, 1991. *J. Atmos. Terr. Phys., 56*, 1227-1234.
59. Jones, W. L. (1969), Ray tracing for internal gravity waves. *J. Geophys. Res., 74*, 2028- 2033.
60. Journal of Atmospheric and Terrestrial Physics (1968), Symposium on upper atmospheric winds, waves and ionospheric drift, *J. Atmos. Terr. Phys.* (Spec. Issue), 30 (5).

Notes

Notes

61. Kaladze, T. D., O. A. Pokhotelov, L. Stenflo, H. A. Shah, G. V. Jandieri (2007), Electromagnetic inertio-gravity waves in the ionospheric E-layer, *Phys. Scr., 76*, 343-.
62. Kanamori, H. (2004), Some fluid-mechanical problems in geophysicswaves in the atmosphere and fault lubrication. *Fluid Dyn. Res., 34*, 1-19.
63. Klostermeyer, J. (1972a), Numerical calculation of gravity wave propagation in a realistic thermosphere, *J. Atmos. Terr. Phys., 34*, 765-774.
64. Klostermeyer, J. (1972b), Comparison between observed and numerically calculated atmospheric gravity waves in the F-region, *J. Atmos. Terr. Phys., 34*, 1393-1401.
65. Klostermeyer, J. (1972c), Influence of viscosity, thermal conduction, and ion drag on the propagation of atmospheric gravity waves in the thermosphere, *Z. Geophys., 38*, 881-890.
66. Krassovsky, V. I. (1972), Infrasonic variations of OH emission in the upper atmosphere, *Ann. Geophys., 28*, 739-746.
67. Kubota, M., H. Kukunishi, and S. Okano (2001), Characteristics of medium- and largescale TIDs over Japan derived from OI 630-nm nightglow observations, *Earth Planets. Space, 53*, 741-751.
68. Kundu, P. K. (1990), Fluid Mechanics, Academic Press, San Diego.
69. Lamb, H. (1908), On the theory of waves propagated vertically in the upper atmosphere, *Proc. London Math. Soc., 7*, 122-141.
70. Lamb, H. (1910), On the atmospheric oscillations, Proc. Roy. Soc. (Ser. A), 84, 551-572.
71. Landau, L. D., and E. M. Lifshitz (1959), Fluid mechanics, Pergamon, New York.
72. Liang, J., W. Wan, and H. Yuan (1998), Ducting of acoustic-gravity waves in a nonisothermal atmosphere around a spherical globe, *J. Geophys. Res., 103*, 11,22911,234.
73. Lighthill, M. J. (1978), Waves in fluids, Cambridge University Press, Cambridge.
74. Lindzen, R. S., and H. L. Kuo (1969), A reliable method for the numerical integration of a large class of ordinary and partial differential equations, *Mon. Weather Rev., 97*, 732-734.
75. Lindzen, R. S., and K.-K. Tung (1976), Banded convective activity and ducted gravity waves, *Mon. Wea. Rev., 104*, 1602-1617.
76. Liu, H.-L. (2007), On the large wind shear and fast meridional transport above the mesopause, *Geophys. Res. Lett., 34*, L08815, doi:10.1029/2006GL028789.
77. Liu, A. Z., and G. R. Swenson (2003), A modeling study of O2 and OH airglow perturbations induced by atmospheric gravity waves, *J. Geophys. Res., 108*, 4151, doi:10.1029/2002JD002474, D4.
78. Liu, A. Z., W. K. Hocking, S. J. Franke, and T. Thayaparan (2002), Comparison of Na lidar and meteor radar wind measurements at Starfire Optical Range, NM, USA, *J. Atmos. Terr. Phys., 64*, 3140.
79. Liu, X., J. Xu, J. Yue, and S. L. Vadas (2013), Numerical modeling study of the momentum deposition of small amplitude gravity waves in the thermosphere, *Ann. Geophys., 31*, 114.
80. Ma, J. Z. G., M. P. Hickey, (2014), Effects of wind shears and nonisothermality on the propagation of acoustic-gravity waves: Attenuation or intensification? *JMSE,* 51 pages, to be submitted.
81. Marks, C. J., and S. D. Eckermann (1995), A three-dimensional nonhydrostatic raytracing model for gravity waves: Formulation and preliminary results for the middle atmosphere, *J. Atmos. Sci.*, 52, 1959-1984 (cited also as ME95 in the text).

82. Martyn, D. F. (1950), Cellular atmospheric waves in the ionosphere and troposphere, *Proc. Roy. Soc.* (Ser. A), 201, 216-234.
83. Mayr, H. G., I. Harris, F. Varosi, and F. A. Herrero (1984), Global excitation of wave phenomena in a dissipative multiconstituent medium, *J. Geophys. Res.*, 89, 10,929-10,959.
84. Mayr, H. G., I. Harris, F. A. Herrero, N. W. Spencer, F. Varosi, and W. D. Pesnell (1990), Thermospheric gravity waves: observations and interpretation using the transfer function model (TFM), *Space Sci. Rev., 54*, 297-375.
85. Mendillo, M., J. Baumgardner, D. Nottingham, J. Aarons, B. Reinisch, J. Scali, and M.C. Kelley (1997), Investigations of thermospheric-ionospheric dynamics with 6300-Å images from the Arecibo Observatory, *J. Geophys. Res., 102*, 7331-7343.
86. Midgley, J. E., and H. B. Liemohn (1966), Gravity waves in a realistic atmosphere, *J. Geophys. Res., 71*, 3729-3748.
87. Mimno, H. R. (1937), The physics of the ionosphere, *Rev. Mod. Phys.*, 9, 1-43.
88. Nappo, C. J. (2002), An Introduction to Atmospheric Gravity Waves, Academic, San Diego, California.
89. Munro, G. H. (1950), Traveling disturbances in the ionosphere, *Proc. Roy. Soc.* (Ser. A), 202, 208-223.
90. Munro, G. H. (1958), Travelling ionospheric disturbances in the F region, *Aust. J. Phys.*, 11, 91-112.
91. Paxton, L. J., D. Morrison, D. J. Strickland, M. J. McHarg, Y. Zhang, B. Wolven, H. Kil, G. Crowley, A. B. Christensen, and C.-I. Meng (2003), The use of far ultraviolet remote sensing to monitor space weather, *Adv. Space Res., 31,* 813-818.
92. Peltier, W. R., and C. O. Hines (1976), On the possible detection of tsunamis by a monitoring of the ionosphere, *J. Geophys. Res., 81*, 1995-2000.
93. Peterson, A.W. (1979), Airglow events visible to the naked eye, *Appl. Opt., 18,* 3390-3393.
94. Picone, J. M., A. E. Hedin, D. P. Drob, and A. C. Aikin (2002), NRLMSISE-00 empirical model of the atmosphere: Statistical comparisons and scientific issues, *J. Geophys. Res.*, 107(A12), 1468, doi:10.1029/2002JA009430.
95. Pierce, J. A., and H. R. Mimno (1940), The reception of radio echoes from distant ionospheric irregularities, *Phys. Rev., 57*, 95-105.
96. Pierce, A. D., and S. C. Coroniti (1966), A mechanism for the generation of acousticgravity waves during thunderstorm formation, *Nature, 210*, 1209-1210.
97. Pitteway, M. L. V., and C. O. Hines (1963), The viscous damping of atmospheric gravity waves, *Can. J. Phys., 41*, 1935-1948.
98. Richmond, A. D. (1978), Gravity-wave generation, propagation, and dissipation in thermosphere, *J. Geophys. Res., 83*, 4131-4145.
99. Roper, R. G. and J. W. Brosnahan (1997), Imaging Doppler interferometry and the measurement of atmospheric turbulence, *Radio Sci., 32*, 11371148.
100. Röttger, J. (1981), Equatorial spread-F by electric fields and atmospheric gravity waves generated by thunderstorms. *J. Atmos. Terr. Phys., 43*, 453-462.
101. Row, R. V. (1967), Acoustic-gravity waves in the upper atmosphere due to a nuclear detonation and an earthquake, *J. Geophys. Res., 72*, 1599-1610.
102. Šauli, P., and J. Boška (2001), Tropospheric events and possible related gravity wave activity effects on the ionosphere, *J. Atmos. Solar-Terr. Phys., 63*, 945-950.
103. Schubert, G., M. P. Hickey, and R. L. Walterscheid (2003), Heating of Jupiters thermosphere by the dissipation of upward propagating acoustic waves, *ICARUS, 163,* 398-413.

Notes

Notes

104. Schubert, G., M. P. Hickey, and R. L. Walterscheid (2005), Physical processes in acoustic wave heating of the thermosphere, *J. Geophys. Res., 110*, DOI:10.1029/2004JD005488.
105. She, C. Y., B. P. Williams, P. Hoffmann, R. Latteck, G. Baumgarten, J. D. Vance, J. Fiedler, P. Acott, D. C. Fritts, and F.-J. Luebken (2006), Observation of anti-correlation between sodium atoms and PMSE/NLC in summer mesopause at ALOMAR, Norway (69N, 12E), *J. Atmos. Sol. Terr. Phys., 68*, 93-101.
106. She, C. Y., D. A. Krueger, R. Akmaev, H. Schmidt, E. Talaat, and S. Yee (2009), Longterm variability in mesopause region temperatures over Fort Collins, Colorado (41N, 105W) based on lidar observations from 1990 through 2007, *J. Terr. Sol. Atmos. Phys., 71*, 1558-1564.
107. Sobral, J. H. A., H. C. Carlson, D. T. Farley, and W. E. Swartz (1978), Nighttime dynamics of the F region near Arecibo as mapped by airglow features, *J. Geophys. Res., 83*, 2561-2566.
108. Sonmor, L. J., and G. P. Klaassen (1997), Toward a unified theory of gravity wave breaking, *J. Atmos. Sci., 54*, 2655-2680.
109. Sun, L., W. Wan, F. Ding, and T. Mao (2007), Gravity wave propagation in the realistic atmosphere based on a three-dimensional transfer function model, *Ann. Geophys., 25*, 1979-1986.
110. Thome, G. D. (1968), Long-period waves generated in the polar ionosphere during the onset of magnetic stroms, *J. Geophys. Res., 73*, 6319-6336.
111. Tolstoy, I. (1963), The theory of waves in stratified fluids including the effects of gravity and rotation, *Rev. Mod. Phys., 35*, 207-230.
112. Tolstoy, I., J. Lau (1971), Generation of long internal gravity waves in waveguides by rising buoyant air masses and other sources. *Geophys. J. Royal Astron. Soc., 26*, 295-.
113. Toman, K. (1955), Movement of the F region, *J. Geophys. Res., 60*, 57-70.
114. Turner, J. S. (1973), Buoyancy Effects in Fluids, Cambridge University Press.
115. Vadas, S. L. (2007), Horizontal and vertical propagation and dissipation of gravity waves in the thermosphere from lower atmospheric and thermospheric sources, *J. Geophys. Res., 112*, A06305, doi:10.1029/2006JA011845.
116. Vadas, S. L., and G. Crowley (2010), Sources of the traveling ionospheric disturbances observed by the ionospheric TIDDBIT sounder near Wallops Island on 30 October 2007, *J. Geophys. Res.*, 115, A07324, doi:10.1029/2009JA015053.
117. Vadas, S. L., and D. C. Fritts (2001), Gravity wave radiation and mean responses to local body forces in the atmosphere, *J. Atmos. Sci., 58*, 2249-2279.
118. Vadas, S. L., and D. C. Fritts (2004), Thermospheric responses to gravity waves arising from mesoscale convective complexes, *J. Atmos. Sol. Terr. Phys., 66*, 781-804.
119. Vadas, S. L., and D. C. Fritts (2005), Thermospheric responses to gravity waves: Influences of increasing viscosity and thermal diffusivity, *J. Geophys. Res., 110*, D15103, doi:10.1029/2004JD005574.
120. Vadas, S. L., and D. C. Fritts (2009), Reconstruction of the gravity wave field from convective plumes via ray tracing, *Ann. Geophys., 27*, 147-177.
121. Vadas, S. L., J. Yue, C.-Y. She, P. A. Stamus, and A. L. Liu (2009), A model study of the effects of winds on concentric rings of gravity waves from a convective plume near Fort Collins on 11 May 2004, *J. Geophys. Res., 114*, D06103, doi:10.1029/2008JD010753.
122. Väisälä, V. (1925), Über die wirkung der windschwankungen auf die pilotbeobachtungen, *Soc. Sci. Fenn. Comment. Phys. Math. II*, 19, 1-46.

123. Vargas, F., G. Swenson, A. Liu, and D. Gobbi (2007), O(^{1}S), OH, and O_2 airglow layer perturbations due to AGWs and their implied effects on the atmosphere, *J. Geophys. Res., 112*, D14102, doi:10.1029/2006JD007642.
124. Vasseur, G., C. A. Reddy, and J. Testud (1972), Observations of waves and travelling disturbances, *Space Res., 12*, 1109-1131.
125. Volland, H. (1969), The upper atmosphere as a multiple refractive medium for neutral air motions, *J. Atmos. Terr. Phys., 31*, 491-514.
126. Waldock, J. A., T. B. Jones (1984), The effects of neutral winds on the propagation of medium scale atmospheric gravity waves at mid-latitudes, *J. Atmos. Terr. Phys., 46*, 217-231.
127. Walterscheid, R. L., and M. P. Hickey (2001), One-gas models with height-dependent mean molecular weight: Effects on gravity wave propagation, *J. Geophys. Res., 106*, 28,831-28,839.
128. Walterscheid, R. L., and M. P. Hickey (2005), Acoustic waves generated by gusty flow over hilly terrain, *J. Geophys. Res., 110*, DOI: 10.1029/2005JA011166.
129. Walterscheid, R. L., G. G. Sivjee, G. Schubert, and R. M. Hamwey (1986), Largeamplitude semidiurnal temperature variations in the polar mesopause: evidence of a pseudotide, *Nature, 324*, 347-349.
130. Wan, W. X., H. Yuan, B. Q. Ning, J. Liang, and F. Ding (1998), Traveling ionospheric disturbances associated with the tropospheric vortexes around Qinghai-Tibet Platcau, *Geophys. Res. Lett., 25*, 3775-3778.
131. Weinstock, J. (1978), Vertical turbulent diffusion in a stably stratified fluid, *J. Atmos. Sci., 35*, 10221027.
132. Whitham, G. B. (1961), Group velocity and energy propagation for three dimensional waves, *Commun. Pure Appl. Math., 14*, 675-691.
133. Wrassea, C. M., T. Nakamura, T. Tsuda, H. Takahashi, A. F. Medeiros, M. J. Taylor, D. Gobbi, A. Salatun, Suratno, E. Achmad, and A. G. Admiranto (2006), Reverse ray tracing of the mesospheric gravity waves observed at 23°S (Brazil) and 7°S (Indonesia) in airglow imagers, *J. Atmos. Solar-Terr. Phys., 68*, 163181.
134. Yeh, K. C., and C. H. Liu (1972), Theory of Ionospheric Waves, Academic, New York.
135. Yeh, K. C., and C. H. Liu (1974), Acoustic-gravity waves in the upper atmosphere, *Rev. Geophys. Space Sci., 12*, 193-216.
136. Yeh, K. C., H. D. Webb (1972), Evidence of directional fltering of travelling ionospheric disturbance. *Nature, 235*, 131-133.
137. Zhong, L., L. J. Sonmor, A. H. Manson, and C. E. Meek (1995), The influence of timedependent wind on gravity-wave propagation in the middle atmosphere. *Ann. Geophys., 13*, 375-394.

Notes

Notes

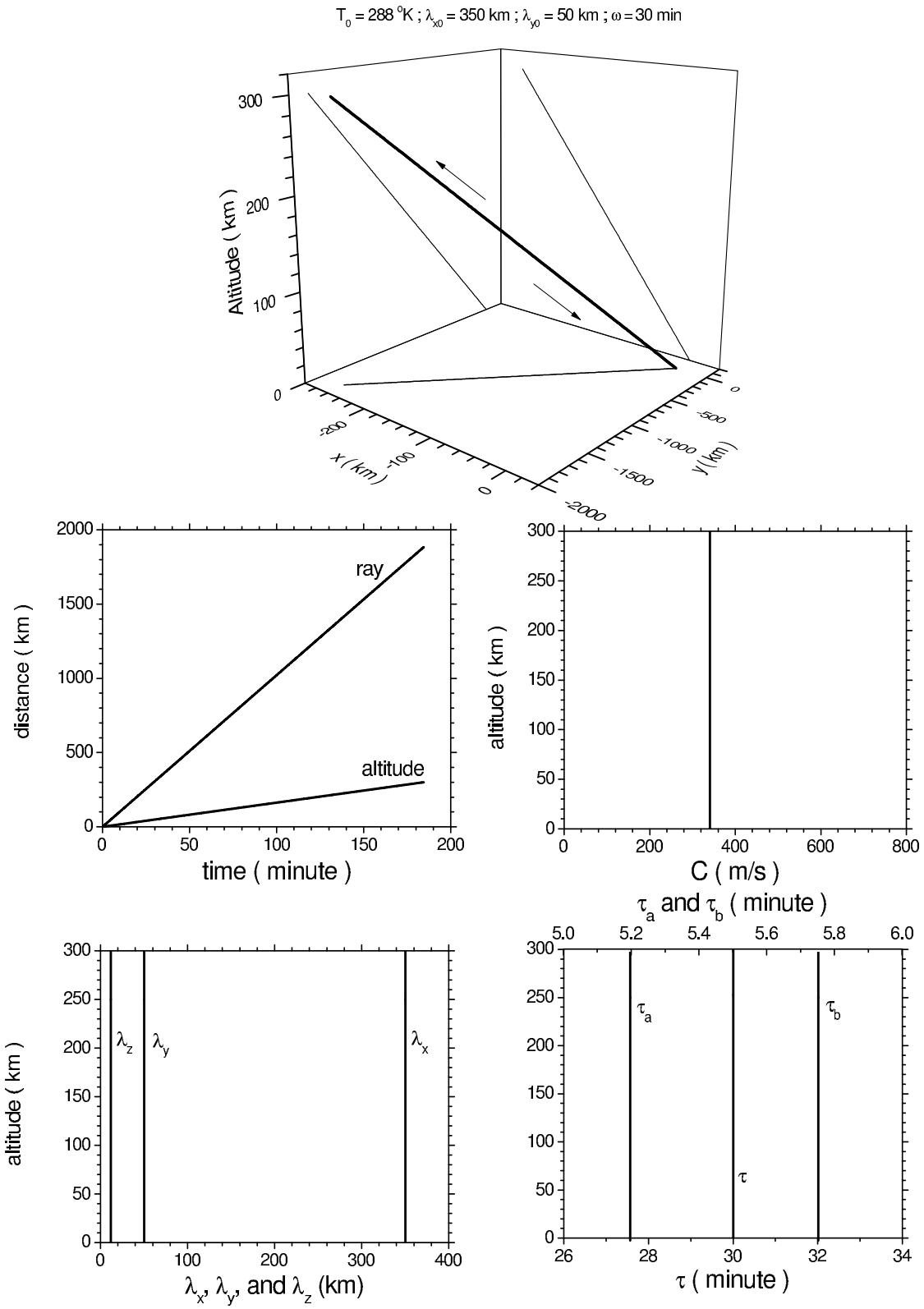

Figure 1 : Case 1: Ray features in hydrostatic, fully isothermal and shear-free atmosphere

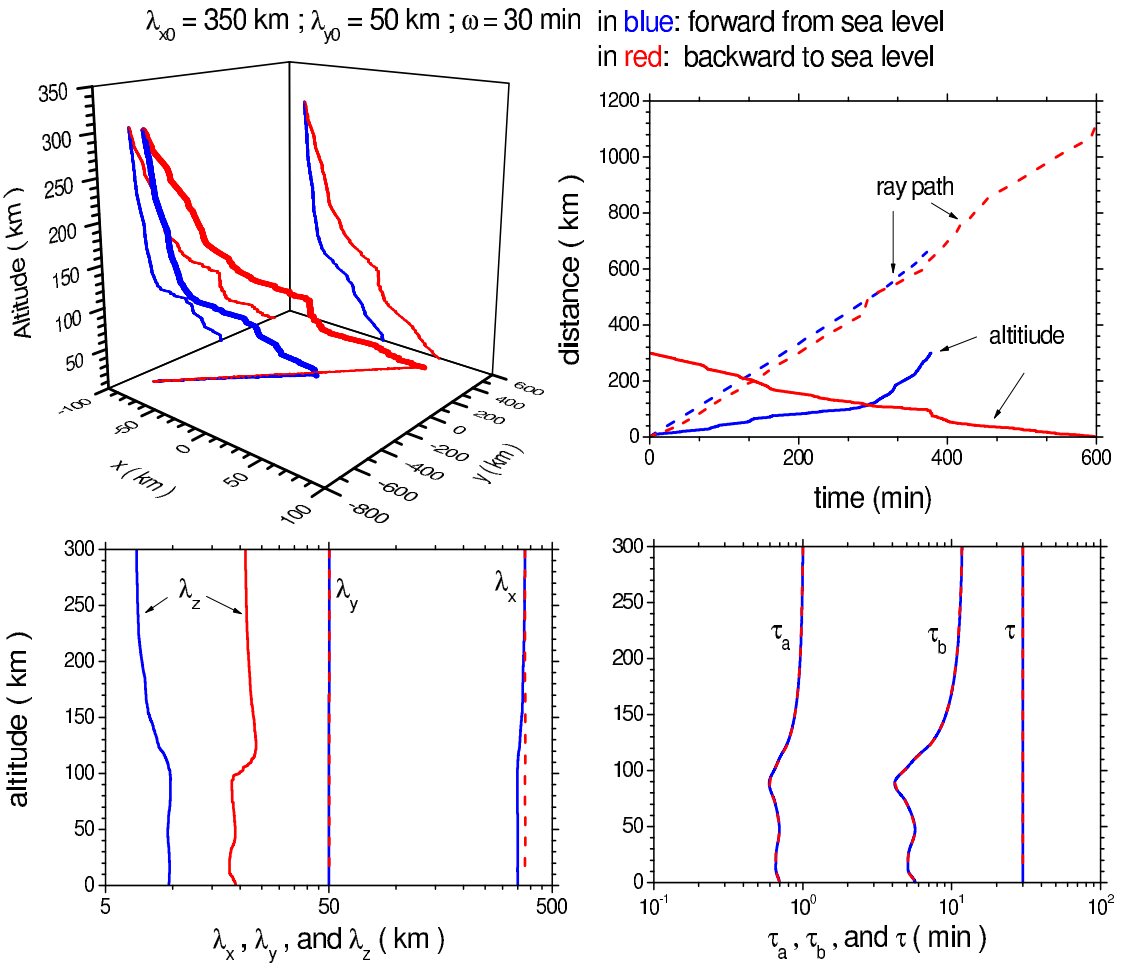

Figure 2 : Case 2-1: Ray propagation in hydrostatic, Hines' locally isothermal and shear-free atmosphere

Notes

Notes

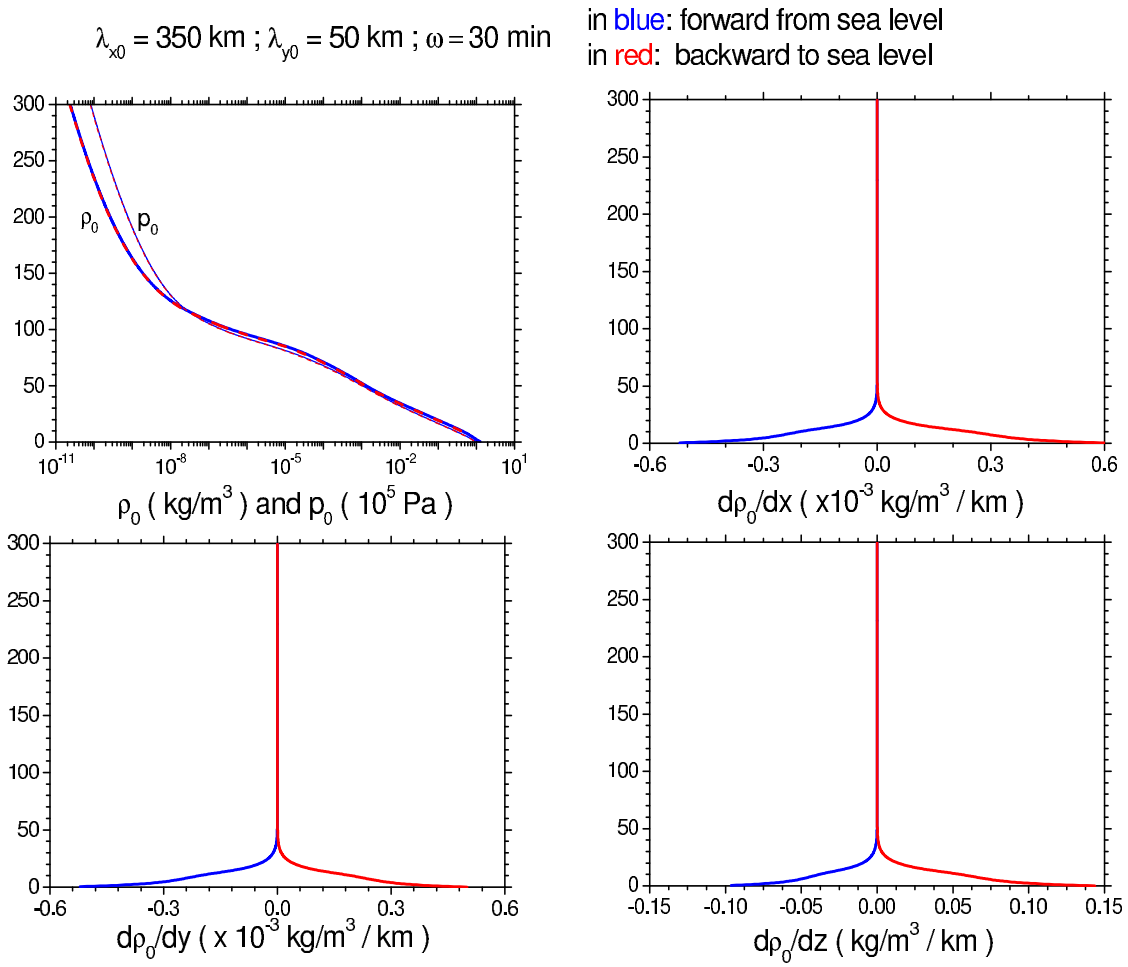

Figure 3 : Case 2-2: Altitude profiles of ˙0 and its gradients, as well as p0, in hydrostatic, Hines' locally isothermal and shear-free atmosphere

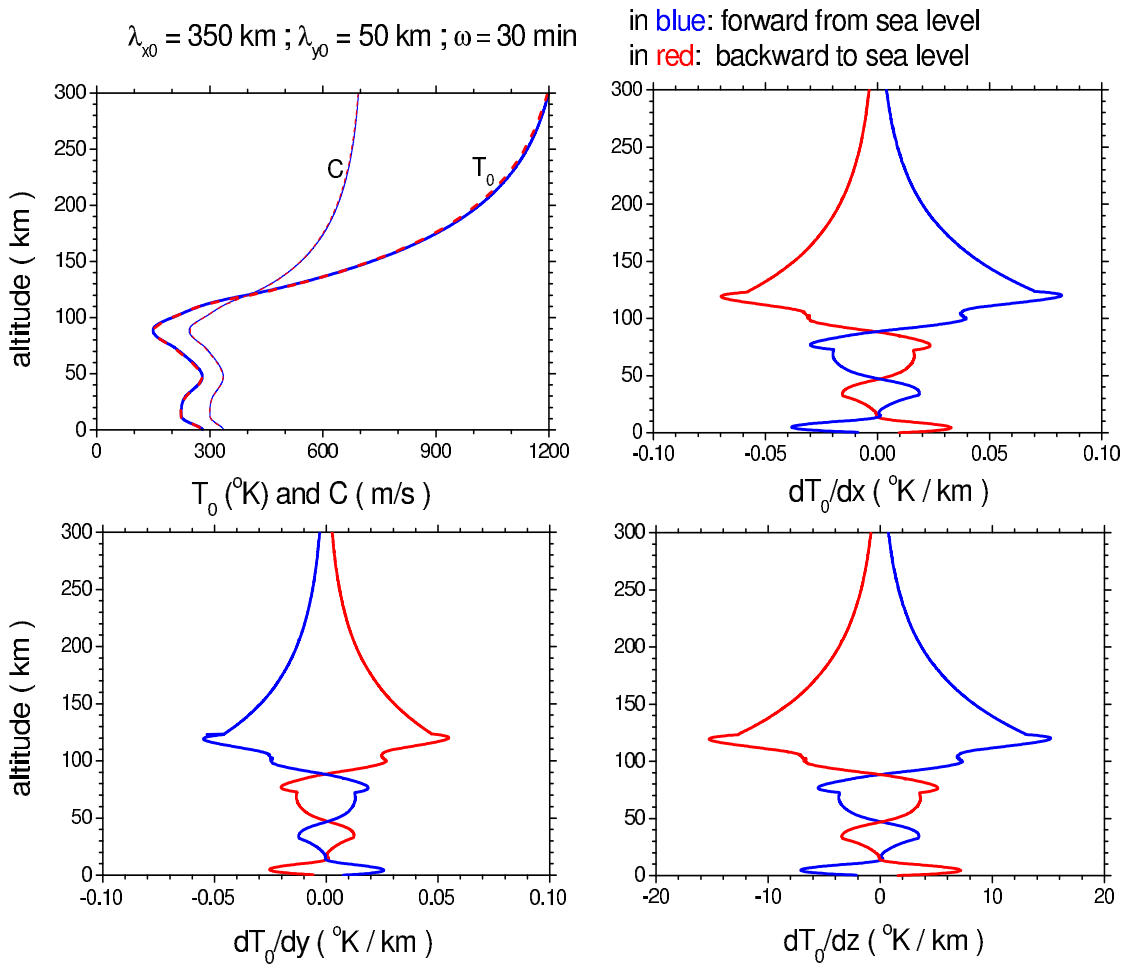

Figure 4 : Case 2-3: Altitude profiles of T_0 and its gradients, as well as C, in hydrostatic, Hines' locally isothermal and shear-free atmosphere

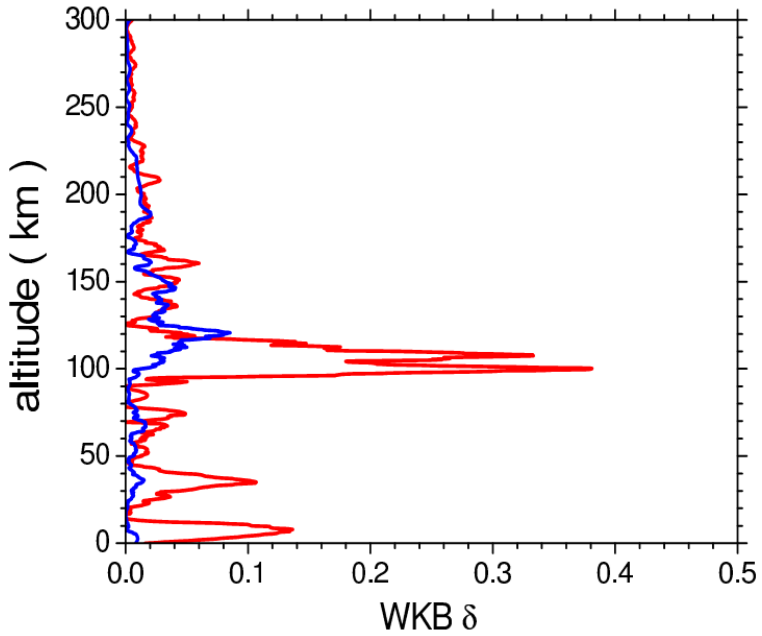

Figure 5 : Case 2-4: Altitude profiles of WKB ˙ in hydrostatic, Hines' locally isothermal and shear-free atmosphere

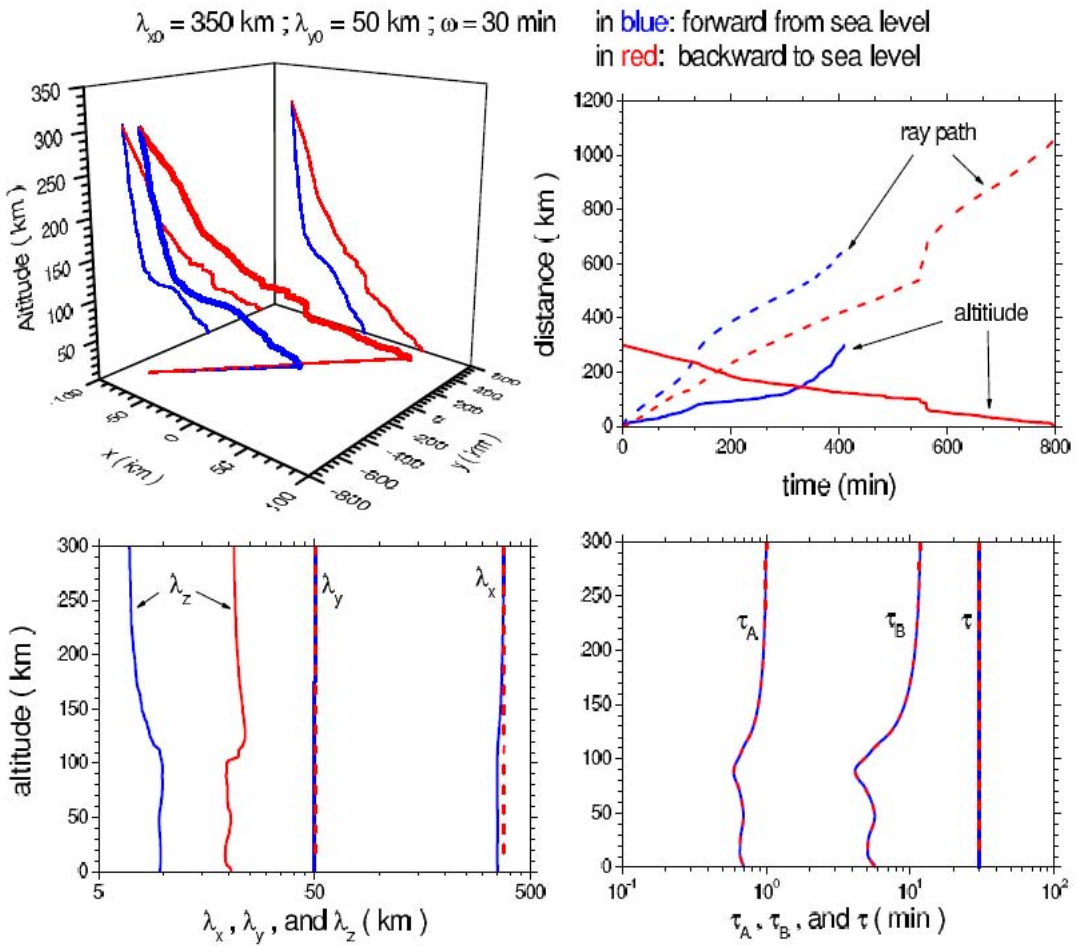

Figure 6 : Case 3-1: Ray propagation in both space (upper left panel) and time (upper right panel), and altitude profiles of wavelengths (lower left panel) and intrinsic wave periods (lower right panel) in hydrostatic, nonisothermal and shear-free atmosphere.

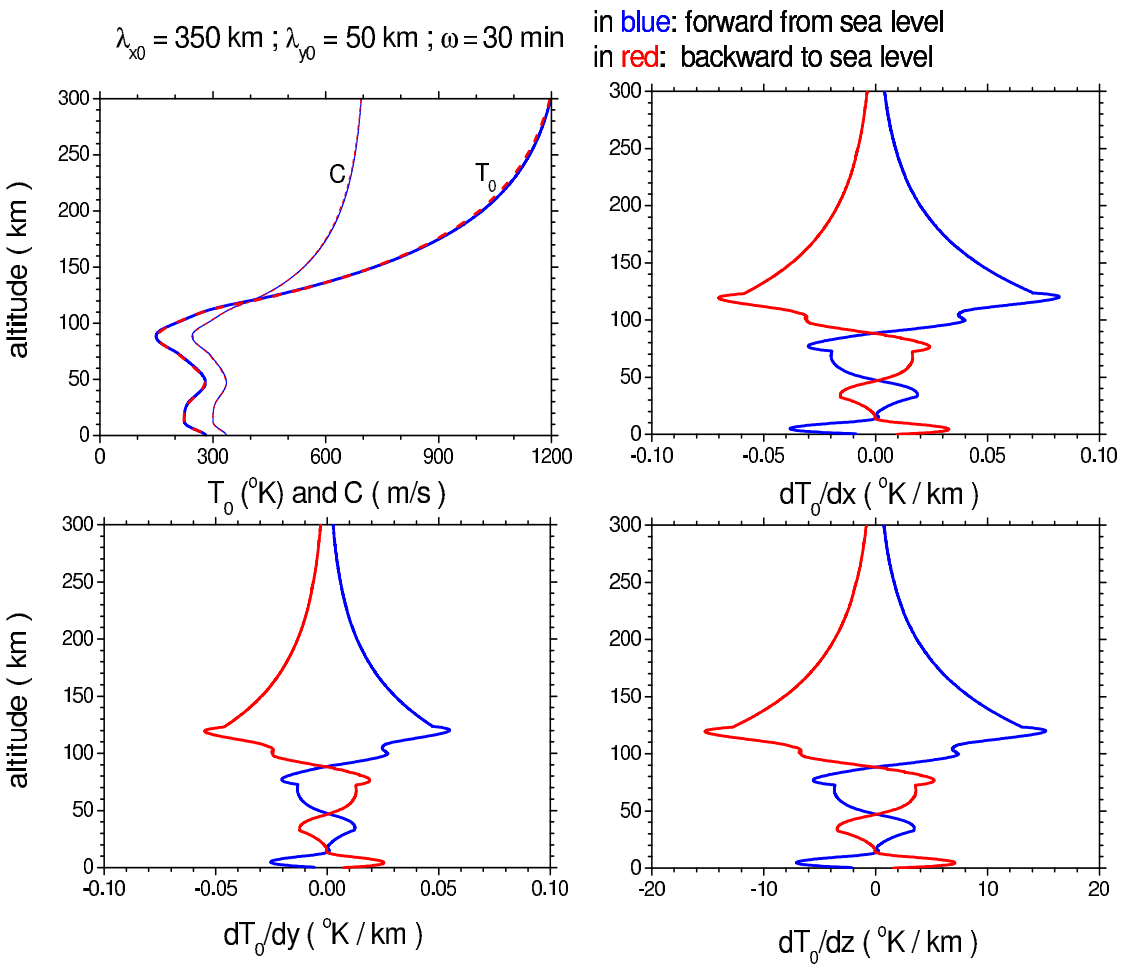

Figure 7 : Case 3-2: Altitude profiles of mean-field temperature (upper left panel) and its gradients in x (upper right panel), y (lower left panel), and z (lower right panel) in hydrostatic, nonisothermal and shear-free atmosphere

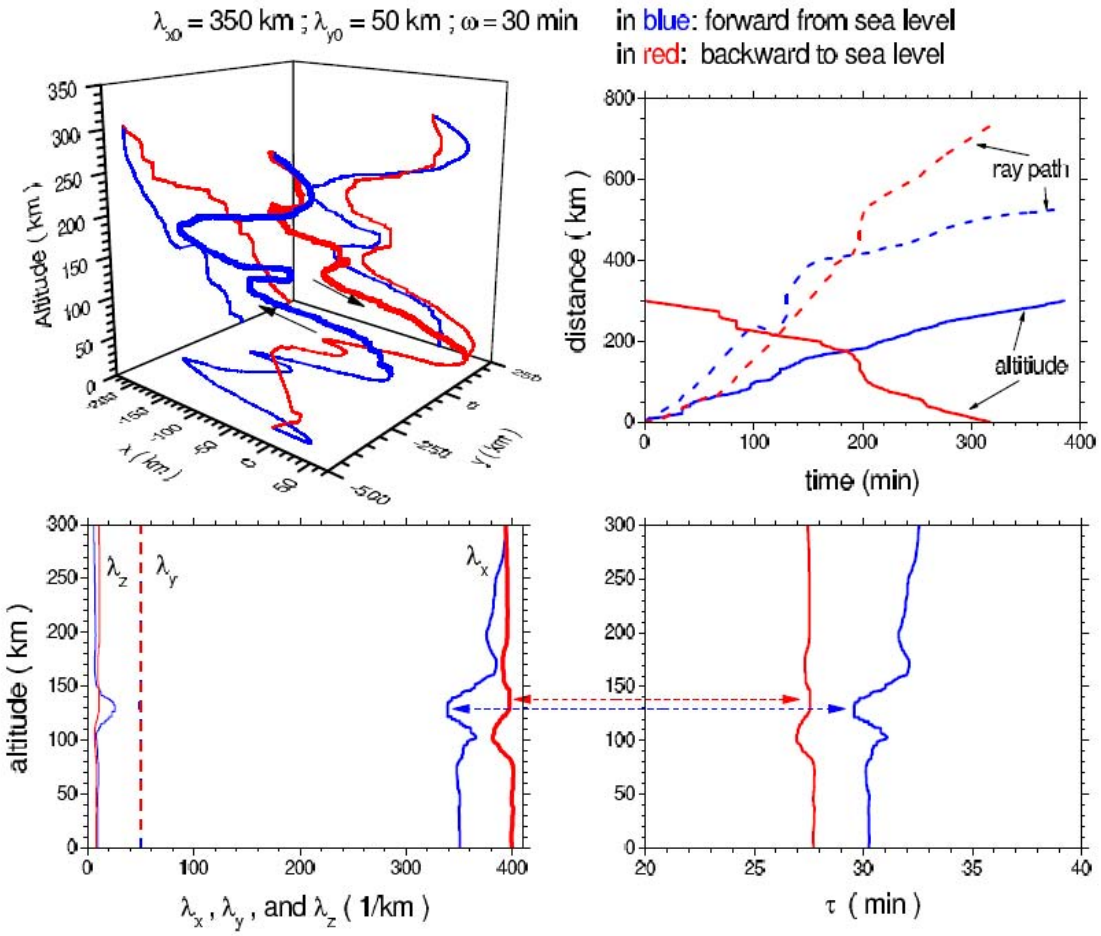

Figure 8 : Case 4-1: Ray propagation in both space (upper left panel) and time (upper right panel), and altitude profiles of wavelengths (lower left panel) and intrinsic wave periods (lower right panel) in isothermal and wind-shearing atmosphere

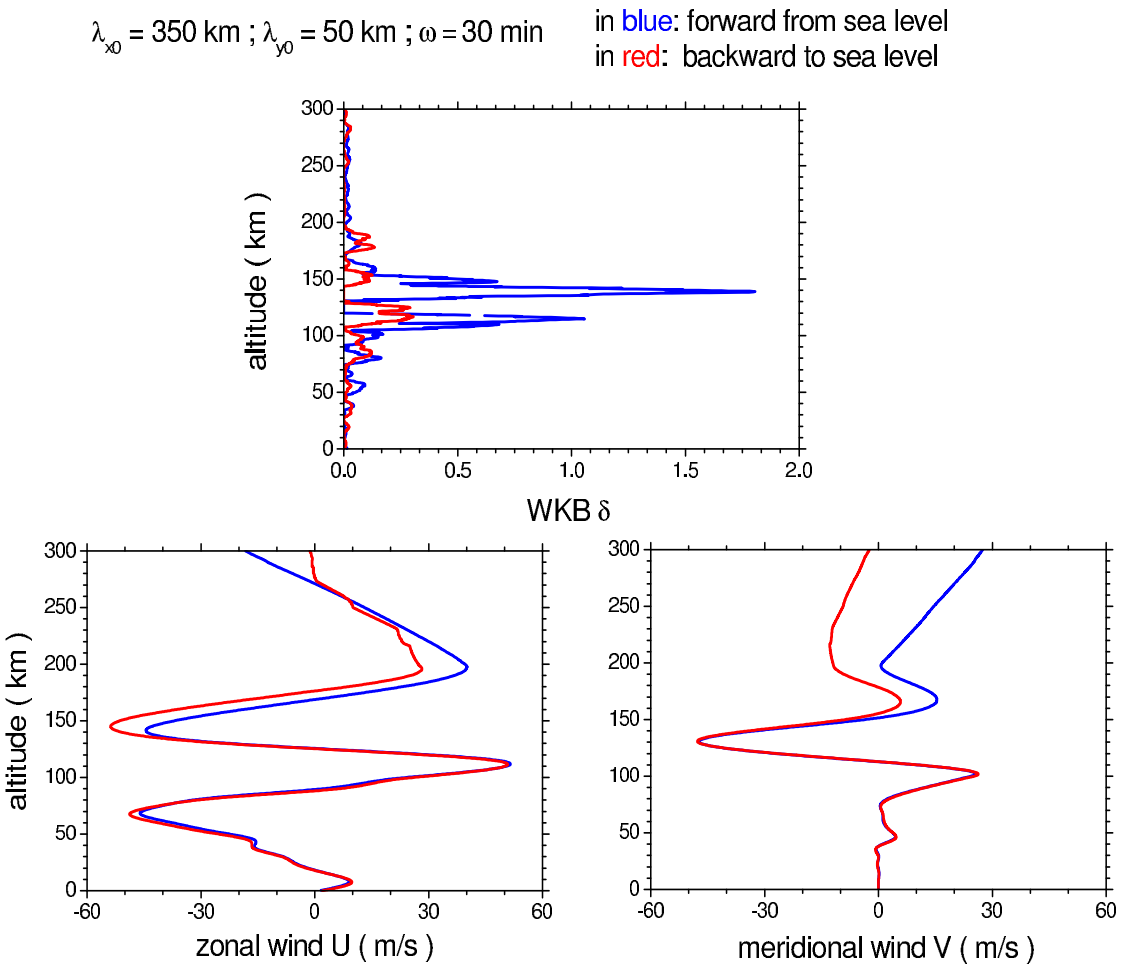

Figure 9 : Case 4-2: Altitude profiles along ray paths of WKB ˙ (upper panel), and mean-field wind (lower left panel: zonal direction; lower right panel: meridional direction) in isothermal and wind-shearing atmosphere

Notes

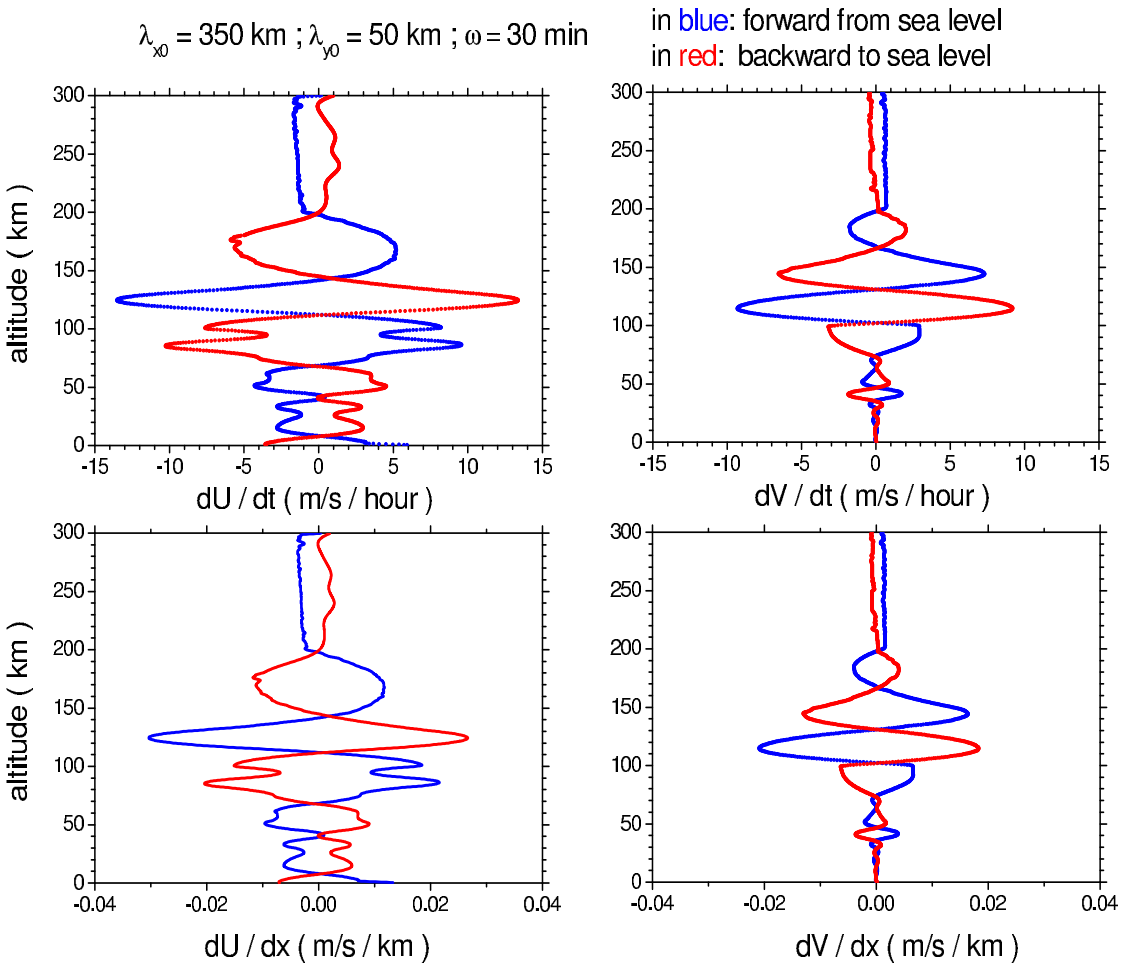

Figure 10 : Case 4-3: Altitude profiles of zonal wind gradients (LHS two panels) and meridional wind gradients (RHS two panels) in t (upper two panels) and x (lower two panels) in isothermal and sheared atmosphere

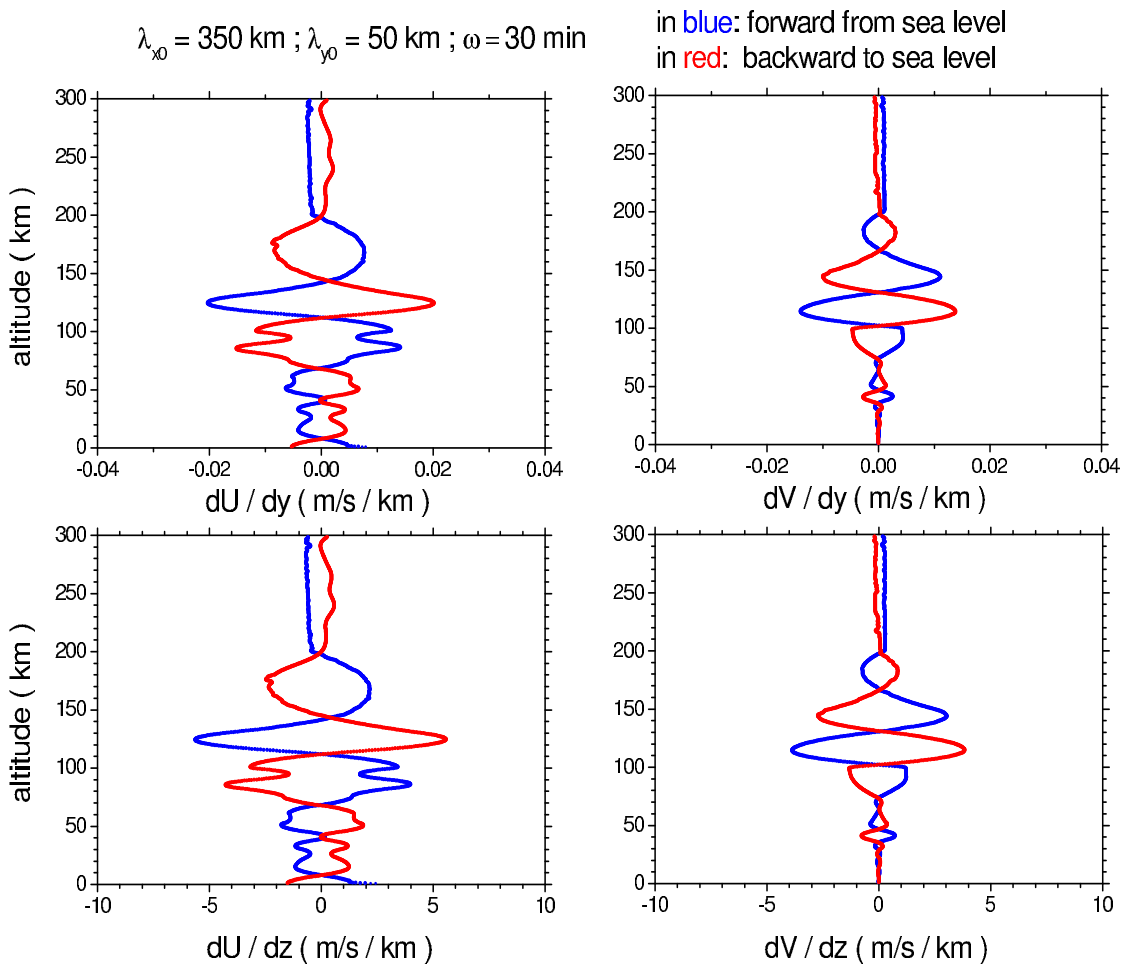

Figure 11 : Case 4-4: Altitude profiles of zonal wind gradients (LHS two panels) and meridional wind gradients (RHS two panels) in y (upper two panels) and z (lower two panels) in isothermal and sheared atmosphere

Notes

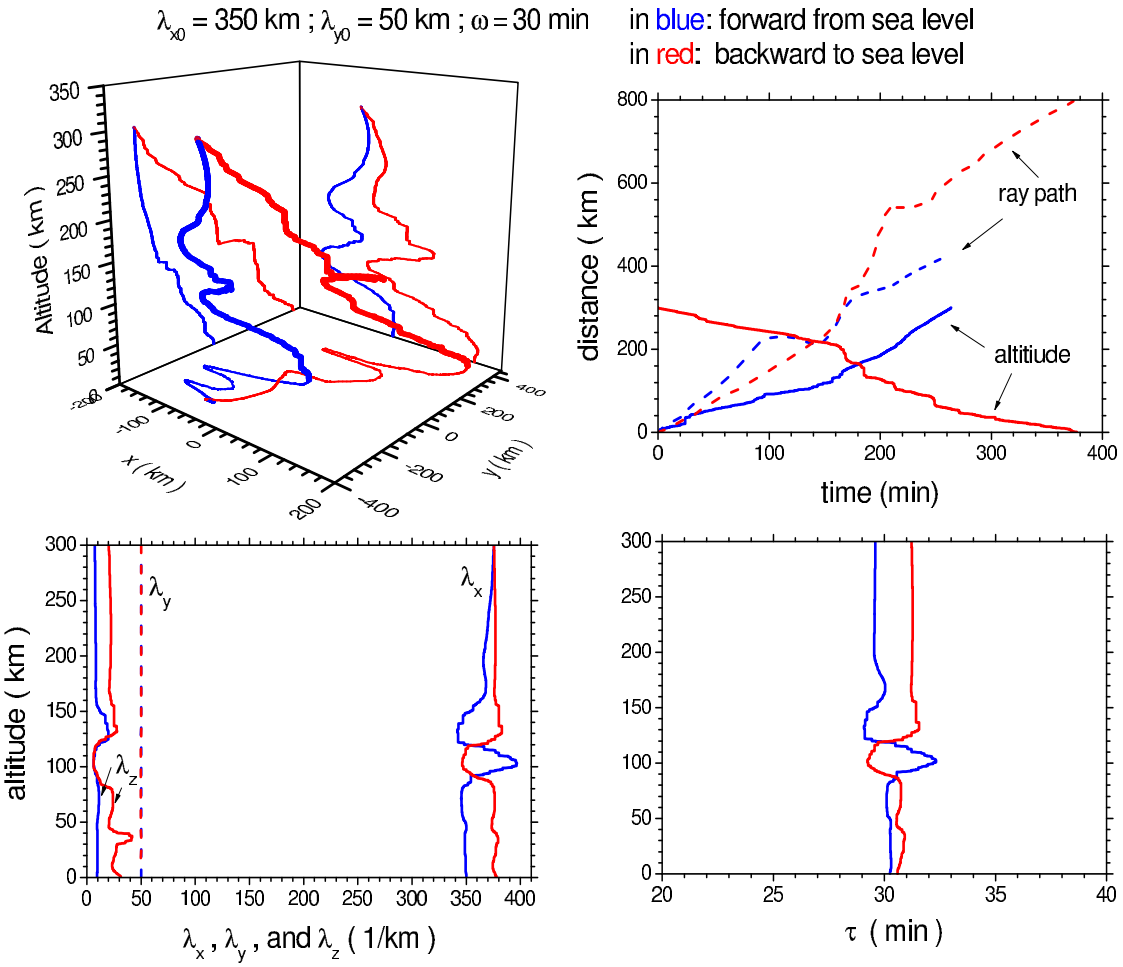

Figure 12 : Case 5-1: Ray propagation in both space (upper left panel) and time (upper right panel), and altitude profiles of wavelengths (lower left panel) and intrinsic wave periods (lower right panel) in nonisothermal and wind-shearing atmosphere

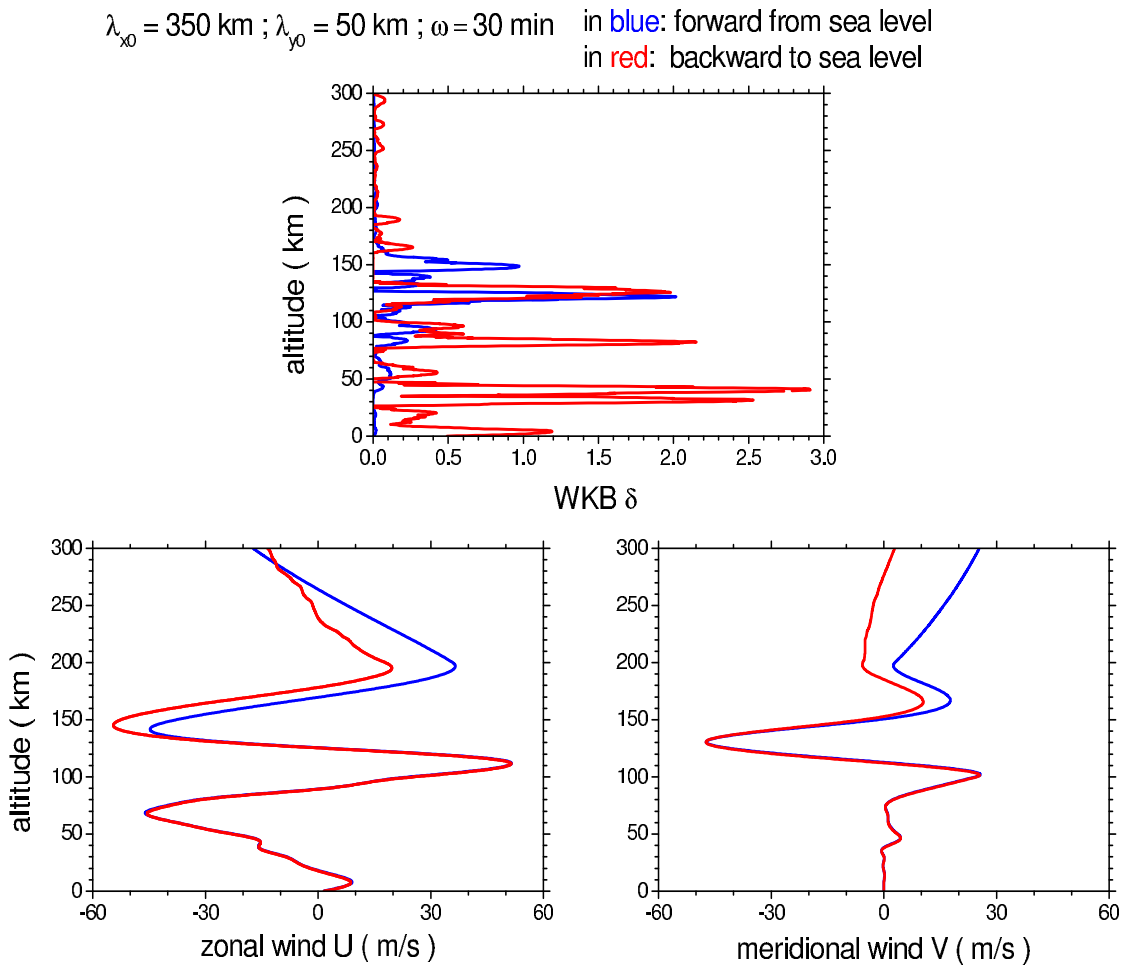

Figure 13 : Case 5-2: Altitude profiles along ray paths of WKB δ (upper panel), and mean-field wind (lower left panel: zonal direction; lower right panel: meridional direction) in nonisothermal and wind-shearing atmosphere

Notes

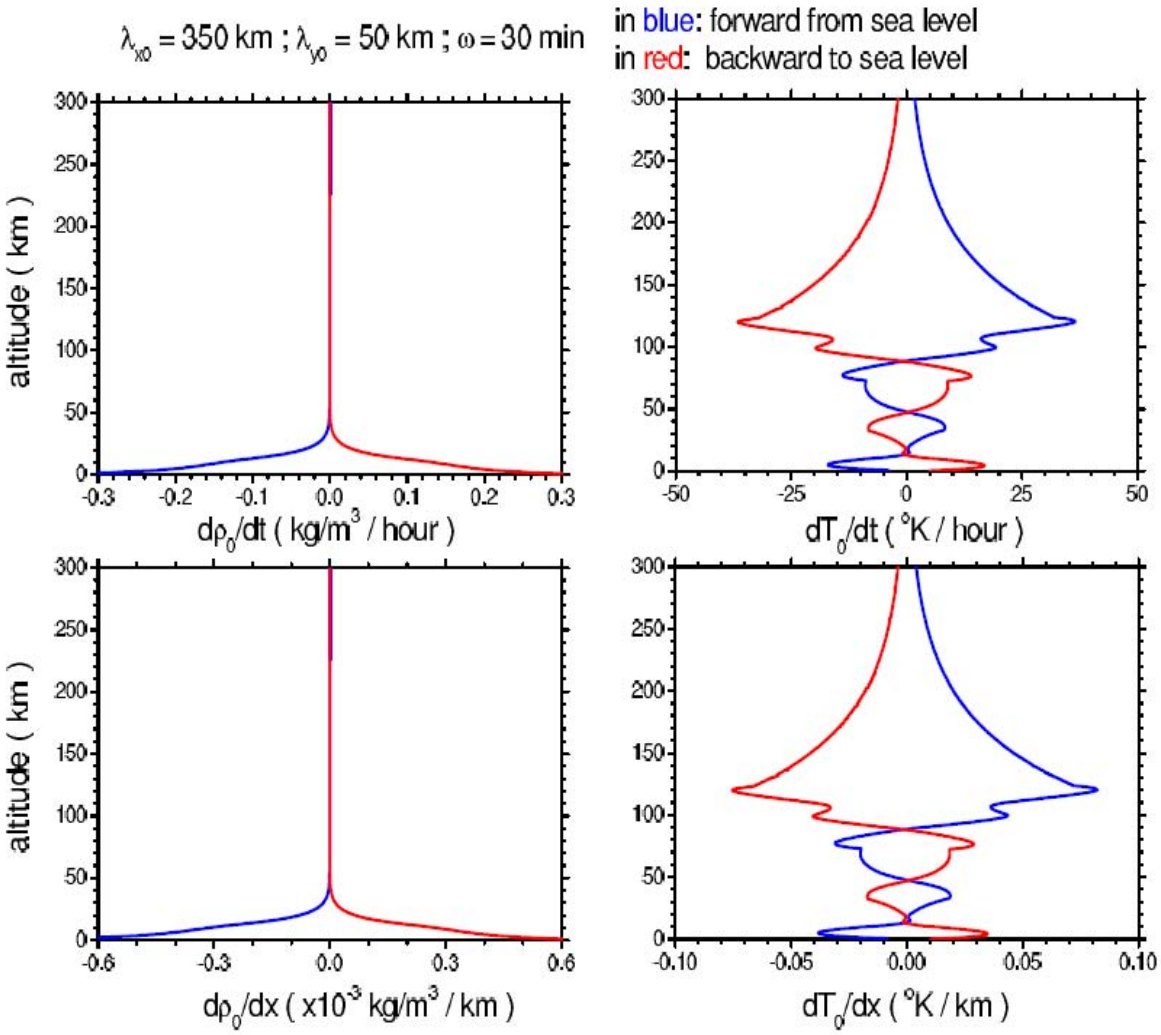

Figure 14 : Case 5-3: Altitude profiles of density gradients (LHS two panels) and temperature gradients (RHS two panels) in t (upper two panels) and x (lower two panels) in nonisothermal and wind-shearing atmosphere

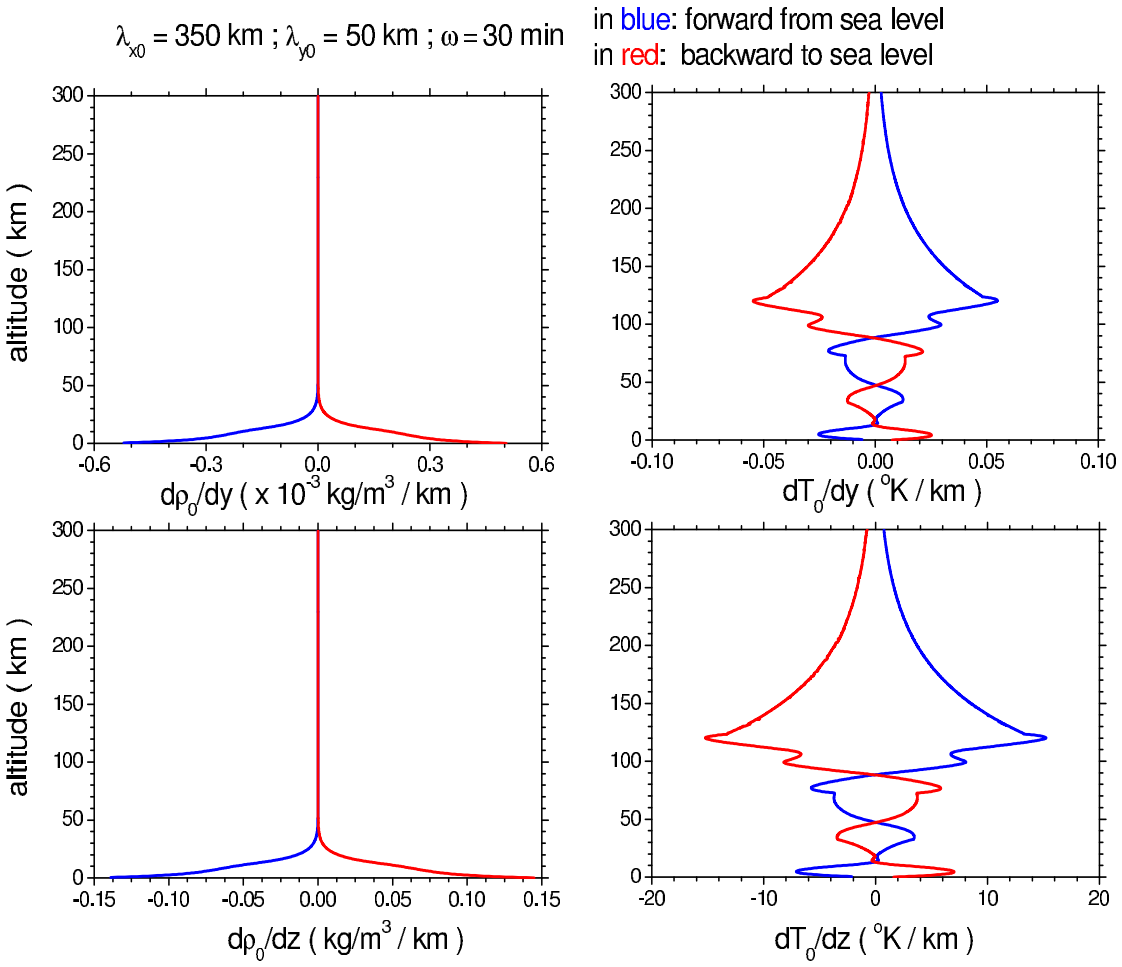

Figure 15 : Case 5-4: Altitude profiles of density gradients (LHS two panels) and temperature gradients (RHS two panels) in y (upper two panels) and z (lower two panels) in nonisothermal and wind-shearing atmosphere

Notes

Notes

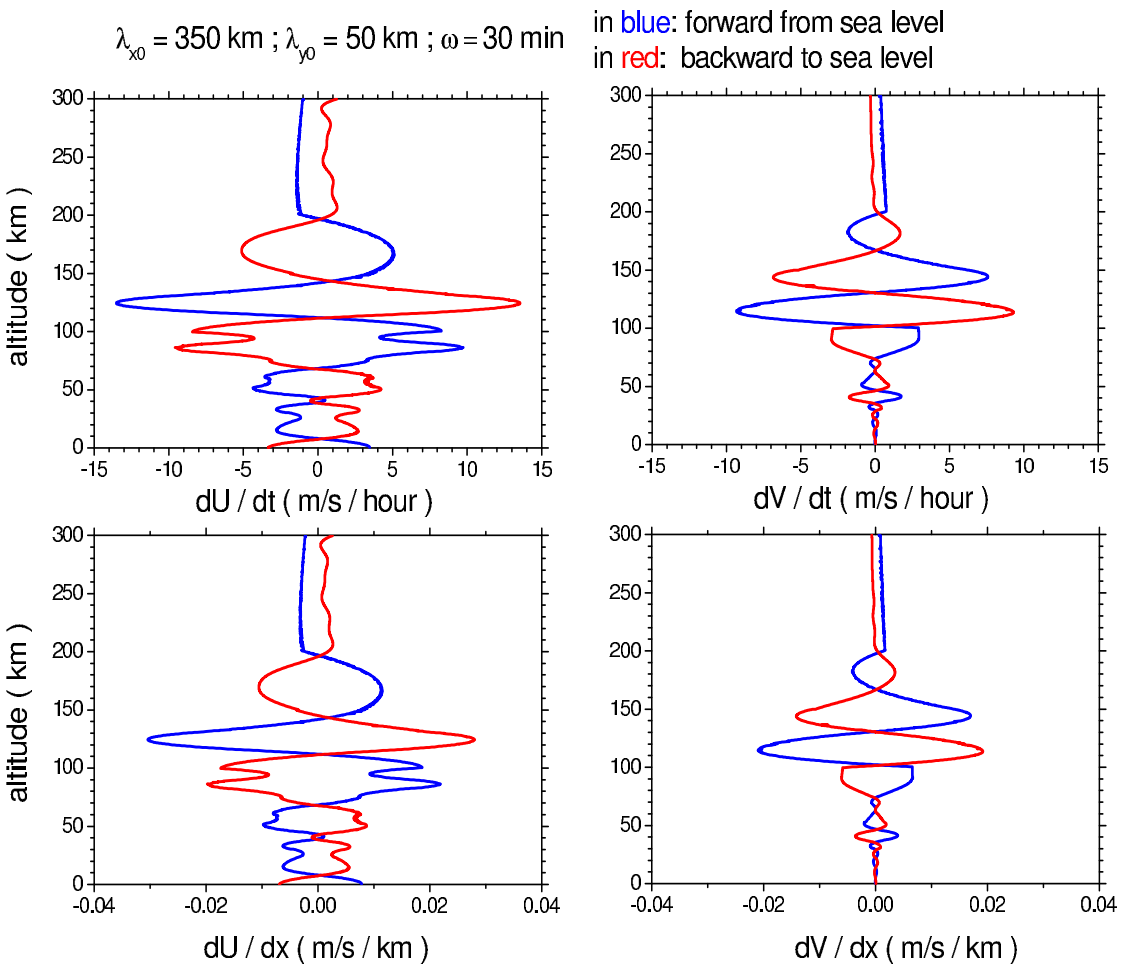

Figure 16 : Case 5-5: Altitude profiles of zonal wind gradients (LHS two panels) and meridional wind gradients (RHS two panels) in t (upper two panels) and x (lower two panels) in nonisothermal and wind-shearing atmosphere

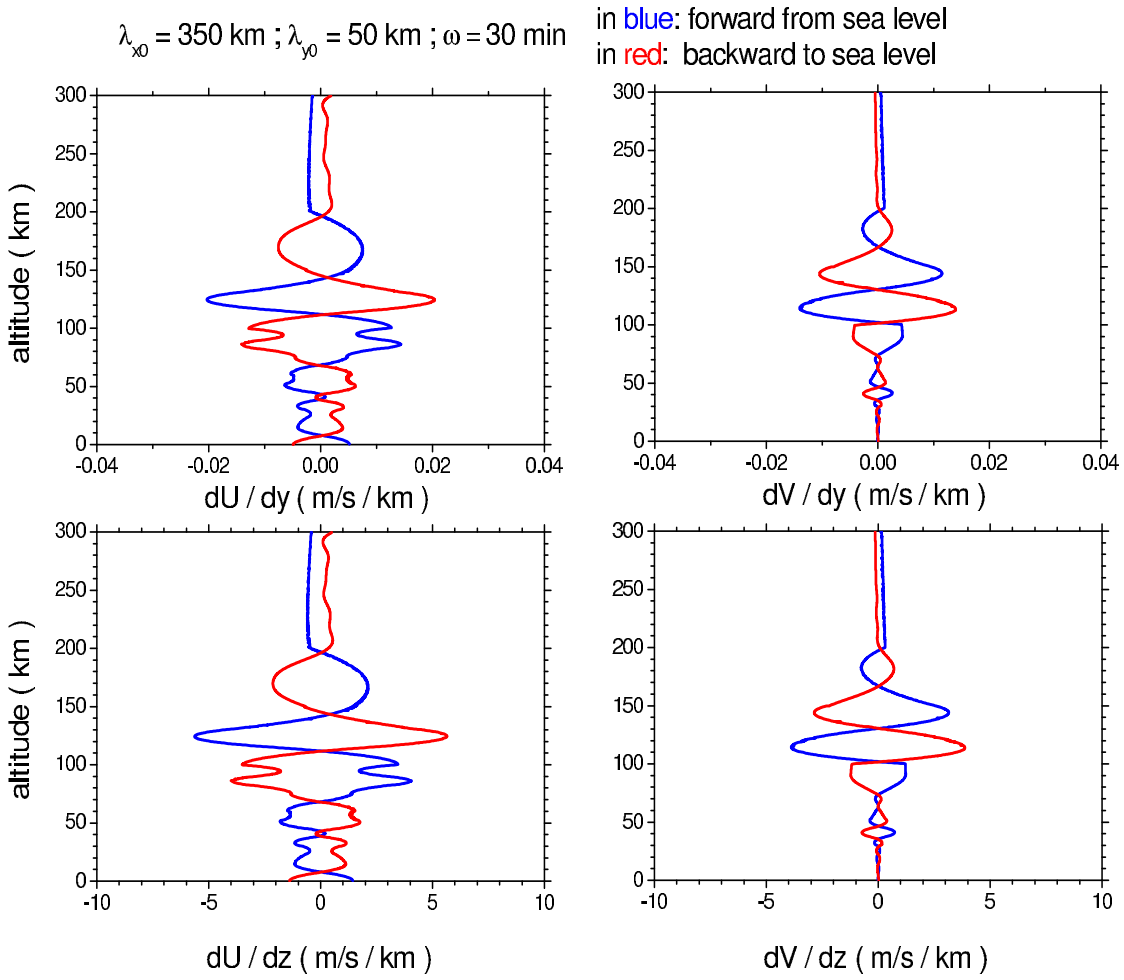

Figure 17 : Case 5-6: Altitude profiles of zonal wind gradients (LHS two panels) and meridional wind gradients (RHS two panels) in y (upper two panels) and z (lower two panels) in nonisothermal and wind-shearing atmosphere

Notes

Notes

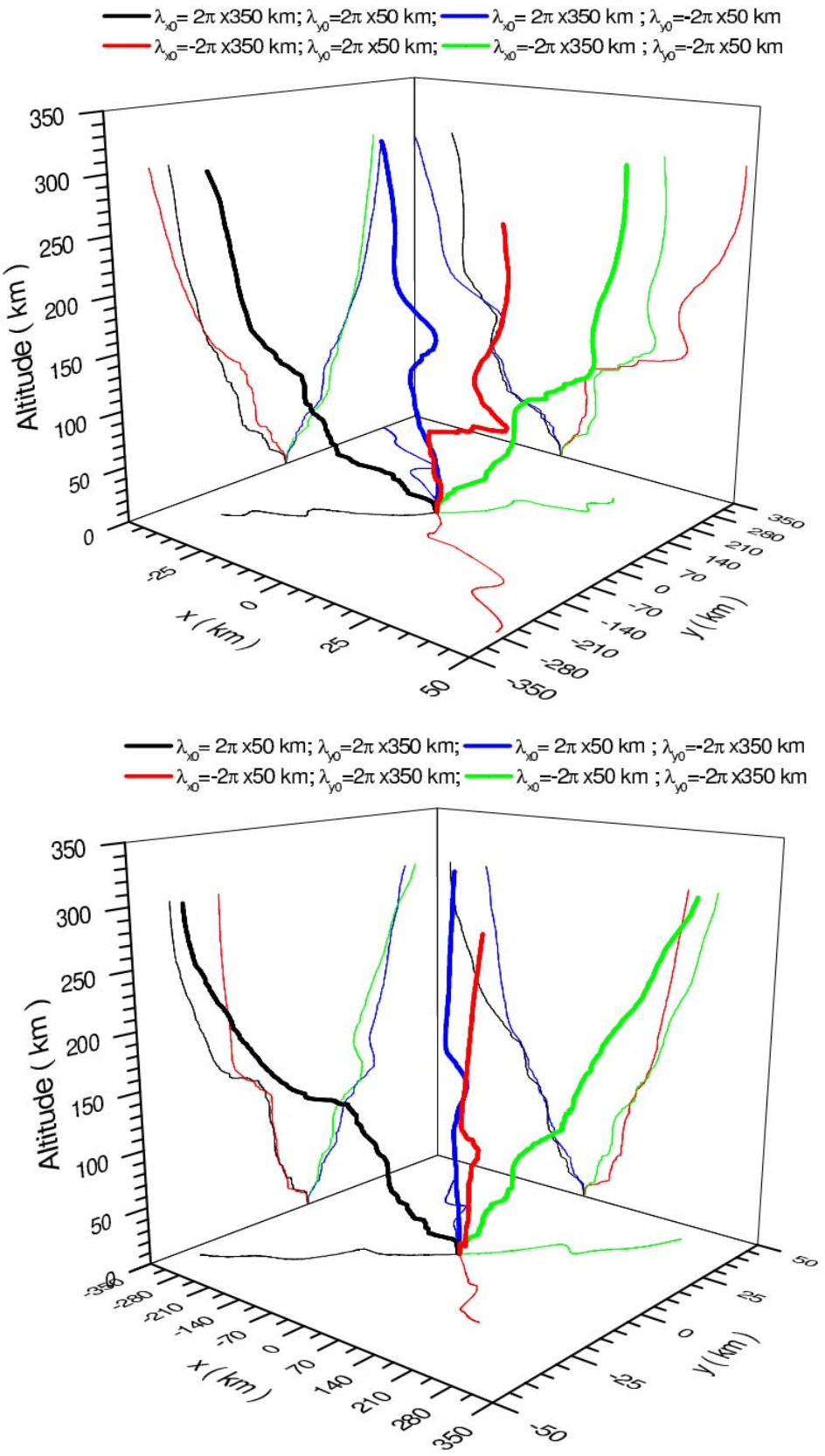

Figure 18 : Case 6-1: Propagating ray paths in space in nonisothermal and windshearing atmosphere under different initial wavelengths

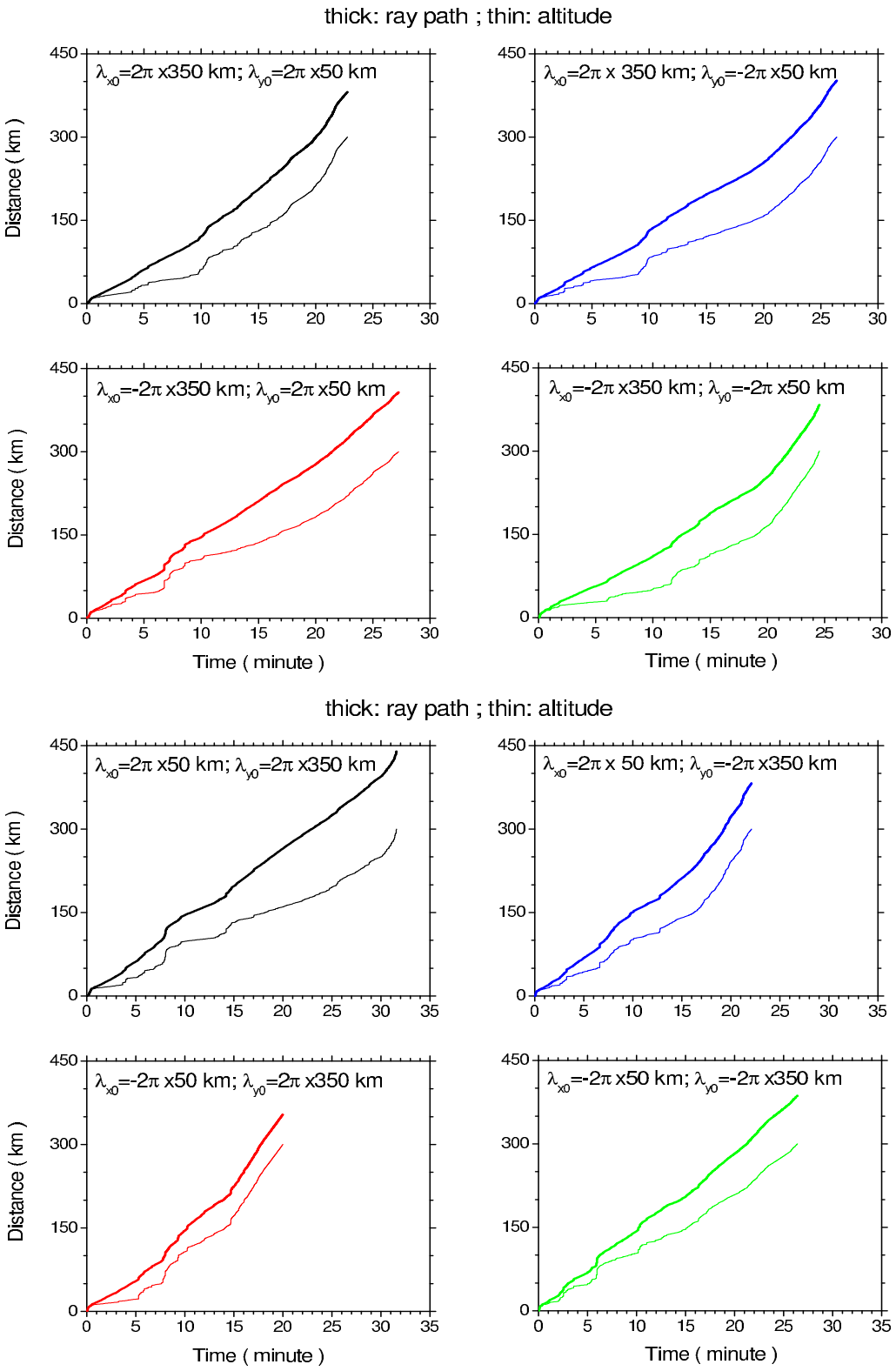

Figure 19 : Case 6-2: the same as Fig.18 but ray paths and vertical increments in time

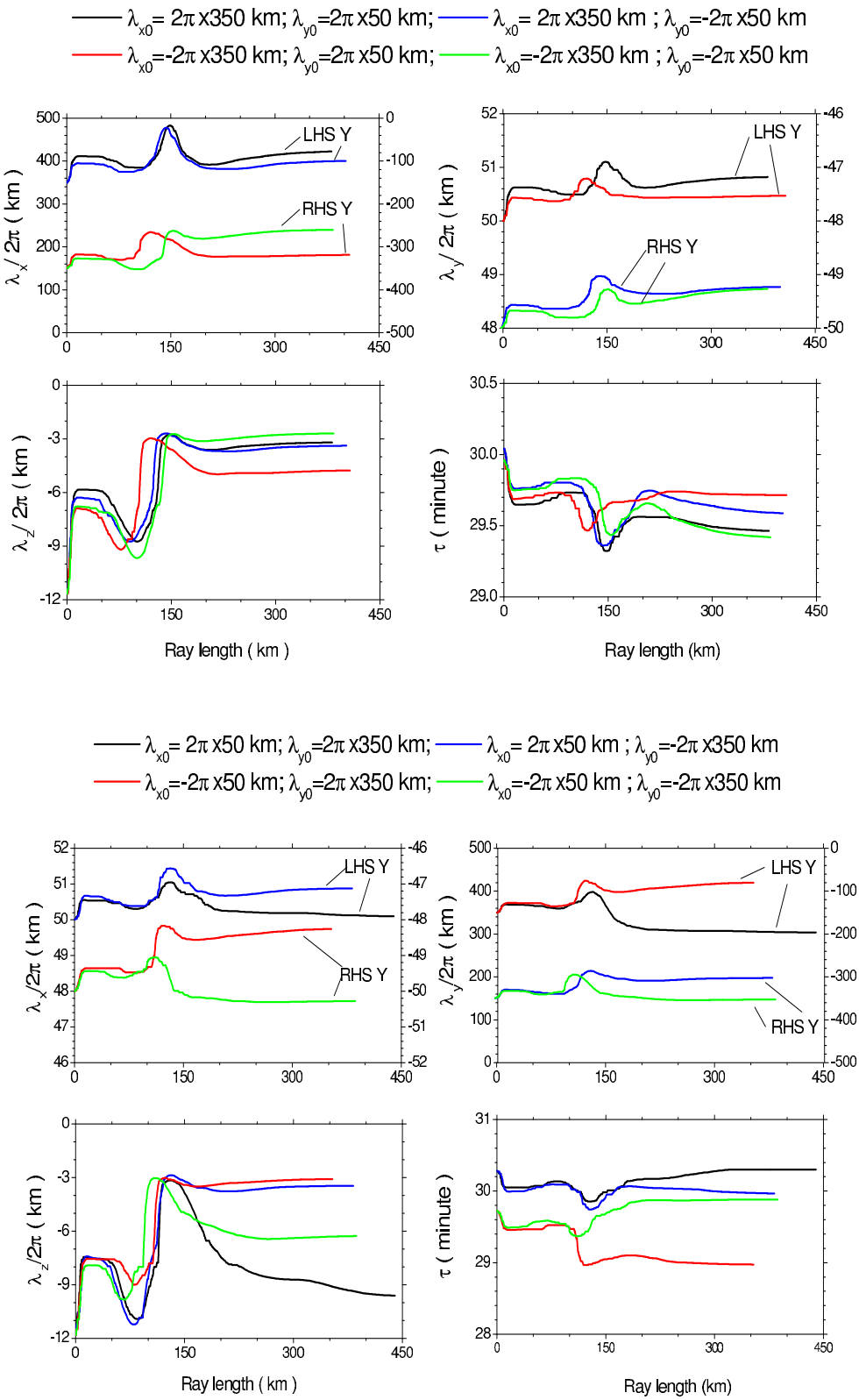

Figure 20 : Case 6-3: Development of $\lambda_{x,y,z}$ and τ versus ray path in wave propagation